arXiv:astro-ph/0106172v1 9 Jun 2001

High Resolution Mid-Infrared Imaging of Infrared Luminous Starburst Galaxies [1]

B. T. Soifer[2], G. Neugebauer, K. Matthews, E. Egami, A. J. Weinberger[3]

Palomar Observatory, California Institute of Technology, 320-47, Pasadena, CA 91125

bts@mop.caltech.edu, gxn@mop.caltech.edu, kym@caltech.edu, egami@mop.caltech.edu,alycia@astro.ucla.edu

M. Ressler

Jet Propulsion Lab, 169-506, 4800 Oak Grove Dr., Pasadena, CA 91109

ressler@cougar.jpl.nasa.gov

N.Z. Scoville

Divison of Physics, Mathematics and Astronomy, California Institute of Technology, 105-24, Pasadena, CA 91125

nzs@astro.caltech.edu

S. R. Stolovy

SIRTF Science Center, California Institute of Technology, 314-6, Pasadena, CA 91125

stolovy@ipac.caltech.edu

J.J. Condon

National Radio Astronomy Observatory, 520 Edgemont Road, Charlottesville, VA 22903

jcondon@nrao.edu

E.E. Becklin

Department of Physics and Astronomy, UCLA, Los Angeles, CA 90095

becklin@astro.ucla.edu,

[1]Based in part on observations obtained at the W. M. Keck Observatory which is operated as a scientific partnership among the California Institute of Technology, the University of California and the National Aeronautics and Space Administration.

[2]Also at SIRTF Science Center, California Institute of Technology, 314-6, Pasadena, CA 91125

[3]Currently at Department of Physics and Astronomy, University of California Los Angeles, 156205 Los Angeles, CA 90095

ABSTRACT

Observations for seven infrared luminous starburst galaxies are reported in the mid-infrared from 8 - 18 μm using the Keck Telescopes with spatial resolution approaching the diffraction limit . All of the galaxies observed show evidence of strong interactions based on optical morphologies. For these galaxies, a substantial fraction, usually more than 50%, of the infrared luminosity is generated in regions ranging in sizes from 100pc – 1 Kpc. Nuclear starbursts often dominate the infrared luminosity, but this is not always true. In some galaxies, most notably NGC 6090, substantial infrared luminosity greatly in excess of the nuclear luminosity is generated in regions associated with the physical interaction between two galaxies. The radio emission is a good tracer of the location of high luminosity young stars.

The visual/ultraviolet radiation output of the nearby star forming galaxies is dominated by emission from regions that are generally not producing the copious infrared luminosity of the systems. As seen in comparing the mid-infrared and near infrared images of the galaxies observed here, the regions of high infrared luminosity in local galaxies are significantly smaller than the galaxies as a whole. The integrated spectral energy distributions (SEDs) of these galaxies are very different from the SEDs of the regions of star formation. If the SEDs of star-forming regions in these galaxies reflect the SEDs that would be found in forming galaxies at high redshift, we would expect the distant galaxies to be dominated by the mid and far-infrared luminosity output far more than the integrated luminous output of nearby starburst galaxies would suggest.

Subject headings: starburst galaxies, luminous infrared galaxies, infrared, galaxies individual: VV114; NGC 1614; NGC 2623; NGC 3690+IC694; IC883=Arp193; NGC 6090; Markarian 331

1. Introduction

Starburst galaxies have long been known to be copious emitters of infrared luminosity. From early observations of nearby starburst systems such as M82 and NGC 253 (see e.g. Kleinmann & Low, 1970, Rieke & Low, 1972, Harper & Low, 1973), it has been clear that the bulk of the energy of these systems emerges in the thermal infrared. Analysis of the IRAS Bright Galaxy Sample showed that 30% of the energy output in the local universe emerges in the mid and far infrared (5 – 200 μm) (Soifer and Neugebauer, 1990) and the bulk of this luminosity is due to star formation in these galaxies. Recently, the idea that the bulk of the radiant energy emitted in the universe has been emitted at infrared wavelengths has been raised through analysis of the far infrared background as measured by the COBE satellite (Hauser et al. 1998, Puget et al. 1996). Further, deep submillimeter surveys have suggested that much of this luminosity is being generated in forming galaxies at redshifts of z$\geq$ 2 (e.g., Eales et al. 2000).

Infrared luminous starbursts in the local universe afford us the best opportunity to study the processes by which such systems form and evolve, and provide detailed examples where we can test physical models of such systems. The IRAS all sky survey (Joint IRAS Science Team, 1989) has provided a unique database from which many such systems have been chosen for detailed examination.

A wide variety of observational techniques have been employed to probe infrared luminous starburst galaxies, ranging from optical spectroscopy (e.g., Kim et al. 1995, Veilleux et al. 1995), mid-infrared imaging and spectroscopy (Keto et al. 1997, Miles et al. 1996, Roche et al. 1991, Dudley 1999) to cm radio continuum imaging (Condon et al. 1990, 1991, hereafter C91). The nuclear environments of starburst galaxies have been effectively imaged with high spatial resolution in the near infrared by e.g. Scoville et al. (2000, hereafter S00), Dinshaw et al. (1999) and Alfonso–Herrero et al. (2000a,b).

Because dust responds through its thermal emission instanteously to the radiation field in which it is embedded, thermal radiation by dust is the ideal way to trace the current location of the dominant luminosity sources, i.e. the most luminous stars, in starbursts. In very dusty systems, such as those known from IRAS observations to be luminous starbursts, high spatial resolution imaging in the thermal infrared can address the location and extent of the current star formation in these galaxies unimpeded by foreground extinction. How the thermal dust emission is related to the other tracers of star-formation is important for utilizing these tracers in more distant galaxies.

IRAS measured the total bolometric luminosity from these galaxies (e.g. Soifer et al. 1987). The spatial resolution of those observations, $\sim 1' - 2'$, was, however, inadequate to locate the emission within the galaxies. Because the mid-infrared wavelengths (8–25 μm) carry a significant fraction of the total bolometric luminosity in infrared bright galaxies, ranging from $\sim$10% to $> 30\%$ of the 8–1000 μm luminosity, observations at these wavelengths with a resolution $\leq 1''$ have the potential to directly trace the locations where the most luminous stars are forming in these systems. With a diffraction limit of $0.24''$ FWHM at 10 μm, the Keck Telescope provides a substantial improvement in spatial resolution over previous mid-infrared observations, probing the distribution of the thermal emission at the 100–300 pc scale in luminous starbursts at distances of 40–120 Mpc.

In this paper we report imaging observations from 8 – 18 μm of a sample of highly luminous starburst galaxies at spatial resolutions of 0.3-0.6$''$. These data provide the highest spatial resolution yet achieved of the thermal emission from these systems and trace the spatial distribution of the emergent luminosity in these systems. For purposes of establishing luminosities and physical distances in these galaxies we adopt H_o=75 km s^{-1}Mpc^{-1}.

2. The Sample

The objects observed were taken from the IRAS Bright Galaxy Sample (BGS, Soifer et al. 1987, 1989) The basic information for the seven objects in the sample is given in Table 1. Since the

goal of this study is to understand luminous starburst galaxies, systems having Seyfert like spectra were excluded. With this selection criterion, there are 25 objects in the BGS in the luminosity range $11.4 \leq \log(L_{bol}[L_{\odot}]) \leq 11.9$; seven were observed. These seven objects are among the closest highly infrared luminous starbusts galaxies. Six of the seven objects observed have clear evidence of strong interactions/mergers from optical images. The only object without such evidence, Markarian 331=UGC 12812, has several close companions. In this luminosity range 60-70% of objects are found in strongly interacting or merging systems (Sanders et al. 1988, Sanders and Mirabel, 1996). The objects were selected to be detectable from the ground at 12 μm, so that there is a bias towards brighter 12 μm flux densities in these galaxies, as measured by IRAS, compared to the galaxies in the same luminosity range in the BGS. Three of the galaxies in the sample, IC 1623=VV114, NGC 3690/IC 694=Arp 299 and NGC 1614=Arp 186 are the three brightest objects at 12 μm in the above sample. This selection of brighter 12 μm flux density appears to be the major bias in our sample as compared to the total BGS sample for this luminosity range.

3. Observations and Data Reduction

The observations were made using the MIRLIN mid-infrared camera (Ressler et al. 1994) at the f/40 bent Cassegrain visitor port of the Keck II Telescope, and the imaging mode of the Long Wavelength Spectrograph (LWS, Jones and Puetter, 1993) at the f/25 forward Cassegrain focus of the Keck I Telescope. In general, only observations where the FWHM of the PSF was less than 1.0″ were used. Because of the variability, the seeing conditions are described throughout the text when specific objects are discussed.

The MIRLIN camera uses a 128×128 Si:As array with a plate scale of 0.138″/pixel for a total field of view of 17″×17″. At each wavelength the observing procedure was the same. A secondary with a square wave chop of amplitude 6″ in the north-south or east-west direction at 4 Hz was employed for fast beam switching. The frames sampling each chop position were coadded separately in hardware, resulting in two images. After an interval of approximately a minute, the telescope was nodded perpendicular to the chop direction (east-west or north-south) by 6″ and a second pair of images was obtained in order to cancel residuals in the sky and to subtract telescope emission. This procedure was repeated a number of times at each wavelength. The data were reduced by differencing the two images obtained within the chop pairs at each nod location. Then the resulting positive images were coadded, with the positions appropriately adjusted to a common location, to yield an image centered in a field approximately 6″×6″. Because of the chopper and telescope nod spacings employed for the observations, the data are not capable of measuring low surface brightness emission that is extended beyond a 6″ diameter region. In addition extended emission within a 6″ region with a surface brightness of 5 mJy/square arcsec is not detectable within these images.

Observations with MIRLIN of VV114, NGC 1614, NGC 3690 and Markarian 331 were obtained in March and October 1998. The MIRLIN observations were made under photometric conditions.

The observations of the targets were interleaved with observations of nearby bright stars that served as photometric calibration and to establish the point spread function (PSF) for the observations.

Observations of all the galaxies listed in Table 1 were made with LWS in October 1999, and January, May and September 2000. Generally these observations were made under photometric conditions. Over the course of the observations, the mid-infrared seeing varied from near diffraction limit($\sim 0.3''$ at 12.5μm) to $> 1.0''$.

The secondary chopper was set to an amplitude of $5''$ at a frequency ~ 5 Hz for all the objects except NGC 1614, NGC 2623, IC 883, where the chopping amplitude was $4''$. Observations were made in a fashion similar to the MIRLIN observations, except that the telescope nodding was in the same direction as the chopping and the nodding amplitude was the same as the chopping amplitude. The data were reduced in a manner similar to the MIRLIN data. The pixel scale is $0.08''$ pixel^{-1}.

The filters defining the photometric bands are quite similar in both MIRLIN and LWS and all have widths about 10 % of the central wavelengths which are listed in Table 2. Details of the filters are given in Soifer et al (1999). The photometry was calibrated based on observations of four bright stars, α Tau=HR 1457 ([12.5 μm]=-3.07 mag), α Boo=HR 5340 ([12.5 μm]=-3.15 mag), β Peg=HR 8775 ([12.5 μm]=-2.55 mag), and α Cet=HR 0911 ([12.5 μm]=-1.92 mag) whose magnitudes, in turn, were based on IRAS and Keck data. The magnitudes adopted at the other mid-infrared wavelengths for these stars were within 0.08 mag of these values. The uncertainties in the photometry, based on the internal consistency of the observations, is estimated to be 5% at $\lambda \leq$17.9 μm. The flux density corresponding to 0.0 mag (Vega-based) was taken to follow the prescription given in the Explanatory Supplement to the IRAS Catalogs and Atlases (Beichman et al. eds, 1989), and is given in Soifer et al. (1999).

In addition, high spatial resolution observations of two of these galaxies, VV114=Arp 236 and NGC 3690=Arp 299 were obtained at 3.2 μm with NIRC (Matthews and Soifer, 1994) on the Keck I telescope in Dec 1996. Although the background is higher at this wavelength than at shorter wavelengths, observations were made in the standard "stare and dither" mode for near infrared observations. Observations were obtained for Markarian 331 at 2.15 μm(K_s) and 3.4 μm (L') using the near infrared camera on the 200-inch Hale Telescope. Observations were made in a similar fashion to those on the Keck Telescope.

4. Results and Discussion for Individual Galaxies

The basic observational results are presented in Table 2 and Figures 1–7. The observed flux densities, measured from the Keck images in the largest beams feasible for each of the galaxies, are presented in Table 2. All of the galaxies were observed at 11.7 and 12.5 μm, while most of them were observed at 17.9 μm. For comparison, the IRAS flux densities at 12μm, representing the integrated flux densities for the galaxies, are also presented in Tabel 2.

In the images, the locations of the origin and in some cases other positions, are marked in each image to facilitate comparisons. Because bright stars are not common in the mid-infrared, the *a priori* astrometric registration of the mid-infrared images with respect to other images is not better than 1 $''$. The locations of the images in these figures were determined by identifying morphologically similar features and assuming that they are spatially coincident at wavelengths between the radio and near infrared. In the mid-infrared morphological features within $\sim 5''$ diameters were imaged on a single array and thus differences on that scale between images at different wavelengths are robust.

In the plots that present the spectral energy distributions (SEDs) for these galaxies, a variety of data are presented. The integrated flux densities at each wavelength are from 2MASS and IRAS data. The large beam Keck data are presented (from Table 2) as well as data from NICMOS (or groundbased images) with the photometry scaled to the same size beams. In addition, to illustrate how the SEDs vary with beam size, we also present multiaperture photometry at the locations where there is significant 12.5μm emission in the Keck images. The beam diameters range from 1$''$ to 4$''$, depending on the size and complexity of the source. Photometry is taken from Keck mid-infrared, NICMOS and groundbased near infrared data. The details of the small beam photometry are explained in the corresponding figure captions.

In the following sections we discuss the observational results for the galaxies separately.

4.1. VV 114=IC1623=Arp 236

At a redshift of cz=6000 km/s (80 Mpc, 400 pc/$''$) VV114=Arp 236 is a highly disturbed system that shows two major centers in optical images, with low surface brightness tails evident over 55$''$ (22 Kpc) in photographic images (Arp 1966). The two centers are aligned east-west and separated by about 20$''$ (8 Kpc). The bolometric luminosity of the system is $\sim 4 \times 10^{11} L_{\odot}$ (Soifer et al. 1987), more than 90% of which emerges at far infrared wavelengths.

Previous detailed near infrared studies of VV114 have been reported by Knop et al. (1994) and Doyon et al. (1995). High resolution near infrared imaging of VV114 has been reported by S00. Radio imaging of this galaxy at 1.4 GHz has been presented by Condon et al. (1990), and at 8.4 GHz by C91. CO observations of VV114 were reported by Yun, Scoville and Knop (1994), while submillimeter continuum imaging of this system is presented in Frayer et al. (1999).

The images presented in Knop et al. (1994), ranging in wavelengths from B(0.44 μm) to L(3.5 μm), show the core of the eastern galaxy is nearly invisible at B and becomes brighter with respect to the western nucleus at longer wavelengths. In the longest wavelength images of Knop et al. the eastern core is clearly double, with a separation between peaks of $\sim$2$''$ (800 pc). In the eastern system the southwestern component becomes increasingly dominant at longer wavelengths. In the L band image of Knop et al. the southwestern component is the only one detected. ISO imaging of this galaxy at 7 μm (Charamandlis et al 1999) shows a bright peak apparently associated

with the eastern nucleus with an extension to the west.

The only portion of the galaxy detected in the MIRLIN and LWS imaging was the eastern source. The 12.5 μm image of this nucleus is presented in Figure 1a, along with the 3.2 μm image obtained with NIRC, the 2.2 μm NICMOS image from S00 and the 8.4 GHz image of C91. The 12.5 μm image presented in Figure 1a is smoothed with a Gaussian with half the diffraction limited FWHM to improve the signal to noise ratio. The effective resolution of this image is 0.34″, i.e. 10% greater than the formal diffraction limit at 12.5 μm.

The two peaks in the eastern nucleus are clearly seen at 12.5 μm; both components are resolved in the image. In the subsequent discussion they are referred to as VV114E$_{NE}$ and VV114E$_{SW}$ respectively. VV114E$_{NE}$ is centrally concentrated with an apparent size of 0.44″. The VV114E$_{SW}$ component is complex, with a main northern component having an apparent size of 0.51″ and several sources to the south, separated from the brighter peak by 0.6″ to 0.8″. The peak positions of VV114E$_{NE}$ and VV114E$_{SW}$, as determined in the NICMOS 2.2 μm image, are marked in all four images of Figure 1a. The marks are located at the same relative positions in all four panels of the montage.

The 3.2 μm image, with lower angular resolution, shows structure that appears quite similar to that at 12.5 μm. At 3.2 μm VV114E$_{SW}$ is only marginally resolved; while VV114E$_{NE}$ is approximately 0.7″ in diameter and apparently at the same orientation as the source seen at 2.2μm. At 3.2 μm VV114E$_{SW}$ appears displaced from the corresponding 12.5 μm source by 0.1″. The radio image shown in Figure 1a shows a general similarity to the 12.5 μm image with a bright isolated northeast component, and a southwest source that consists of several distinct components separated by ∼0.4–0.8″. The radio map of VV114E$_{SW}$ shows that the components are reasonably close in peak brightness, like the 12.5 μm image.

At 2.2 μm the structure of VV114E is significantly different from the mid-infrared and radio structure. VV114E$_{NE}$ shows a significant ellipticity at 2.2 μm, with a FWHM size of 0.8″× 0.4″ at a position angle of 60 °, suggestive of a stellar nucleus. VV114E$_{SW}$ breaks up into two sources, a bright, apparently unresolved source nearly coincident in position with the 12.5 μm source, and a fainter source 0.86″ to the southwest of the brighter point-like source.

While consistent in overall structure, the images do not agree in detail at the different wavelengths. The registration between images at different wavelengths is based on the *assumption* that VV114E$_{NE}$ is spatially coincident at all wavelengths. Since this source is reasonably compact and isolated from other sources by ∼ 2″ at all wavelengths, we believe that this is a reasonable assumption.

At 2.2 μm and 3.2 μm the positions of VV114E$_{NE}$ and VV114E$_{SW}$ agree in position angle to <1 °and in separation to within 0.03″. In addition, as noted above, at 3.2 μm the northeastern source appears slightly elongated in the same sense as the elliptical shape of this source at 2.2 μm. There is also a slight distortion of the lower level contours of the southwestern source at 3.2 μm consistent with a fainter source at the location of the faint source to the southwest of the point

source in the 2.2 μm image. Thus given the angular resolution and signal to noise ratio in the 3.2 μm image, these images appear the same.

The 12.5 μm and 2.2 μm images differ in detail. In both cases the northeastern source is extended, and there is some suggestion of extended emission at 12.5 μm at a similar position angle as the major axis of the 2.2 μm image. There is a significant disagreement in position and morphology of the southwestern source between these wavelengths. This is illustrated in Figure 1b, where the 12.5 μm contours are overlaid on a grayscale version of the 2.2 μm image. The northeast and southwest peaks in the two images appear at the same position angle of 80 °but the location of the brightest component of the southwestern source disagrees by 0.1″ between the two wavelengths. Furthermore, the secondary peaks to the south and southwest of the southwestern peak at 12.5 μm do not appear to have any corresponding peaks in the 2.2 μm image, while the faint peak to the southwest of the bright 2.2 μm peak has no counterpart in the 12.5 μm image.

The largest discrepancies in location of the peaks are between the 12.5 μm image and the 8.4 GHz image. As can be seen in Figure 1a, the separations between the VV114E$_{NE}$ and VV114E$_{SW}$ peaks differ by 0.3″ or 100 pc. There is no *a priori* means of knowing whether the registration we have chosen (forcing VV114E$_{NE}$ to coincide at both wavelengths) is valid, or whether forcing the peak of VV114E$_{SW}$ to coincide might be appropriate. In either case, a discrepancy exists between the locations of the mid-infrared and radio peaks.

Figure 1b also shows the 12.5 μm and the 3.2 μm contours overlaid separately on a grayscale version of the 8.4 GHz image. In both cases the location of the peak of the southwestern source in the "thermal" infrared does not coincide with the radio peak. As in the case of comparing the sources at 12.5 μm and 2.2 μm, the northeast and southwest peaks fall along the same position angle, but the separations disagree. The separation of the radio peaks is 1.35″, compared to 1.55″ in the thermal infrared. The structure to the south of the southwestern peak appears to agree much better between the radio and mid-infrared images, showing agreement in both location and elongation.

In summary, *assuming* VV114E$_{NE}$ is spatially coincident at all wavelengths, the VV114E$_{SW}$ peaks coincide at 2.2 and 3.2 μm, and are displaced from the 12.5 μm peak by 0.1″ (30 pc). The 12.5 μm peak is displaced from the 8.4GHz peak by 0.2″(80pc); at 12.5 μm VV114E$_{SW}$ lies between the 8.4 GHz and 2.2/3.2 μm peaks, and they all lie on the same line from VV114E$_{NE}$.

The flux density of VV114 measured by IRAS at 12 μm is 0.8 Jy in an unresolved beam and 1.1 Jy in total. The flux density measured in the imaging of VV114E is 0.34 Jy at 12.5 μm, significantly less than the IRAS values. To attempt to detect additional emission, the position of peak extended infrared emission in VV114W based on the ISO image of Laurent et al. (2000) was imaged as well. This location is 14″ west of the VV114E position. No flux was detected in the Keck image at 12.5 μm, with a limit of 8±5 mJy in a 4″ diameter beam. For this imaging the chopping amplitude was 10″. The non-detection of the western source places an upper limit of ∼1mJy/square ″ on the surface brightness of the emission at this location.

The western galaxy in the VV114 pair is detected at 3.2 μm, and is shown in Figure 1c. The full field containing both systems is shown at 2.2 μm and 3.2 μm, where the 3.2 μm contours are overlaid on the 2.2 μm grayscale. The 3.2 μm NIRC image shows that there is low surface brightness, extended emission associated with the western galaxy and the interaction region between the two galaxies. The 3.2 μm emission is comprised of a combination of photospheric, nebular and dust emission. The 3.2 μm filter includes the 3.3 μm feature commonly identified as due to Polycyclic Aromatic Hydrocarbons, or PAHs (e.g., Dale et al. 2000) and so there is a contribution from this mechanism as well. The detection of extended emission at 3.2 μm, in addition to the detection of substantial extended emission in the IRAS photometry with a $\sim 1'$ beam, argues that the non-detection of the majority of the IRAS 12 μm flux is probably the result of the difficulty in detecting low surface brightness extended emission in the thermal infrared.

The spectral energy distributions for the sources in VV114 from 1.2 to 25μm are presented in Figure 1d as flux per octave (νf_ν). In addition to the total fluxes from IRAS and 2MASS, photometry in a $4''$ diameter beam centered on VV114E, as well as in $1''$ diameter beams centered on VV114E$_{NE}$ and VV114E$_{SW}$, are presented to illustrate how the SEDs change with observing beam. The small beam photometry at 2.2μm was scaled from the NICMOS image in S00, while the 3.2μm data are from our NIRC imaging. The lower panel illustrates the photometry at the corresponding location in VV114W.

Both VV114E$_{NE}$ and VV114E$_{SW}$ show a significant drop in flux at 10 μm as compared to the observed flux at 8 and 12 μm. This is generally attributed to absorption by cold silicate dust overlaying warmer emission. A substantial uncertainty in quantifying the overlaying absorption arises from the contribution to the underlying emission from the aromatic (PAH) features. The spectrum of VV114 reported by Dudley (1999) with a $5.5''$ diameter beam includes all of the emission seen in the image in Figure 1a. This spectrum shows an emission feature at 11.3 μm (rest wavelength) attributed to PAH emission. The spectrum of Dudley, if smoothed to the resolution of the filters used for our imaging, is consistent with the apparent ratio of fluxes at 11.7 and 12.5 μm as shown for the flux from VV114E in the large beam shown in Figure 1d.

The separate spectral energy distributions (SEDs) of VV114E$_{NE}$ and VV114E$_{SW}$ differ significantly. The decrease in flux density at 10 μm of VV114E$_{NE}$ is substantially deeper than in VV114E$_{SW}$. The composite mid-infrared spectrum of galaxies presented by Dale et al. (2000), if representative of the underlying emission spectrum for VV114E, suggests that the extinction of an intrinsic PAH like spectrum would lead to an absorption optical depth of about 0.5 at 10 μm in VV114E$_{SW}$. This is also consistent with the fact that the southwest source appears to dominate the VV114E flux throughout most of the 10 μm wavelength range. VV114E$_{NE}$ appears to have an optical depth τ in the range 1–2 greater than that of VV114E$_{SW}$ at 9.7 μm (i.e. a net differential optical depth, τ, of 1.5–2.5 at $\sim$10 μm). The absorption optical depths cited here are by comparison to zero absorption at 8 or 12 μm.

Yet another complication is the fact that the dust optical depth is not zero at 8 and 12 μm,

as assumed above. Li and Draine (2000) have recently compiled the properties of interstellar dust opacity (predominantly due to silicate absorption) that would result in an increase of a factor of 1.3 to the optical depths derived above to take into account the extinction at 8 and 12 μm.

Thus we infer that the silicate optical depths are ~ 0.7 and 2–3 for VV114E$_{SW}$ and VV114E$_{NE}$ respectively. These results, which imply VV114E$_{NE}$ is more heavily obscured than VV114E$_{SW}$, contradict the extinctions derived from the near infrared imaging of these sources. As can be seen directly from Figure 1 of Knop et al. (1994), VV114E$_{SW}$ is significantly "redder" than VV114 NE, i.e., it becomes significantly brighter than VV114 NE at 2.2 μm compared to 0.8 μm. To the extent that this reflects overlaying extinction, it suggests substantially more extinction obscuring VV114E$_{SW}$ than VV114E$_{NE}$.

4.2. NGC 1614=Arp 186

NGC 1614 is a strongly interacting galaxy at a redshift of cz=4800 km/s (64 Mpc, 320 pc/$''$). The optical photograph of Arp (1966) shows crossed tails with a total extent of $\sim$30 Kpc. Its infrared luminosity is $4 \times 10^{11} L_{\odot}$ (Soifer et al. 1987). A detailed visible, infrared and radio study by Neff et al. (1990) shows an HII optical spectrum and tidal tails. The radio image at 5 GHz shows a ring $\sim 1.2''$ (380 pc) in diameter (Neff et al.). High resolution near infrared imaging and spectroscopy (Alonso-Herrero et al. 2000b) shows a starburst nucleus of $\sim$0.3$''$ (100pc) diameter revealed through strong photospheric CO absorption in supergiants. This nucleus is surrounded by a ring of very large HII regions. The ring diameter of $\sim$1.2$''$(380 pc) is traced in the Pα image (Alonso-Herrero et al.). Miles et al. (1996) have reported imaging of NGC 1614 at 11.7 μm with 1$''$ resolution.

Figure 2a shows the 12.5 μm contour map of NGC 1614, the 4.8 GHz radio contours of Neff et al (1990), the 2.2 μm broadband and the 1.87 μm Pα NICMOS images from Alonso-Herrero et al.(2000b). The 12.5 μm image, obtained in excellent (diffraction limited) 0.30$''$ seeing, shows a ring-like structure of diameter $\sim$1.2$''$ and overall extent of $\sim$1.7$''$ that appears virtually identical in overall appearance to the ring seen in the radio at 4.8 GHz and in Pα.

A detailed comparison of the 12.5 μm and the Pα and 4.8 GHz images is presented in Figure 2b, where the contours of the mid-infrared image are overlaid on the grayscale images of Pα and 4.8 GHz radio emission. The images were superimposed by matching by eye the centroids at the different wavelengths. The peaks in the thermal infrared, Pα and 4.8 GHz images are very well matched, particularly to the southeast where the peaks agree in size and orientation.

In contrast to the mid-infrared and Pα images, the 2.2 μm continuum image (Figure 2a) does not reveal a ring like structure. Rather the 2.2 μm continuum shows a strong central peak, with an overall size similar to the size of the mid-infrared image. This results from the fact that the 2.2 μm light traces the stars which peak at the nucleus, while the mid-infrared, radio and Pα images trace the ring of current star fomation.

Figure 2c shows the SED of NGC 1614, comparing the photometric measurements obtained with the Keck images in 2″ and 4″ diameter beams, and the IRAS observations. This plot shows that the Keck observations detect ∼87% of the flux measured at 12 μm with IRAS in a 4″ beam, and 72% of the IRAS 12 μm flux in a 2″ beam. The photometry shows that the mid-infrared emission is predominantly confined to a nuclear region $\sim 1.7''$ (550 pc) in diameter (FWHM) with <30% of the emission extending outside this diameter. The mid-infrared spectrum presented in Roche et al. (1991) shows a suggestion of both PAH emission and silicate absorption. We do not have adequate photometric data to distinguish PAH emission from silicate absorption. The images at 11.7 and 12.5 μm show similar structure, showing that grossly there are not significantly different spectra in different locations in the starburst region.

4.3. NGC 2623=Arp 243

NGC 2623=Arp 243 is a strongly interacting galaxy at a redshift of cz=5535 km/s (74 Mpc, 370pc/″) with an infrared luminosity of $3 \times 10^{11} L_{\odot}$ (Soifer et al. 1987). The optical image (Arp, 1966) shows two opposing tidal tails extending over 120″ (45 Kpc). Near infrared NICMOS imaging (S00) shows a single bright nucleus and surrounding galaxy, and the 8.4 GHz image (C91) shows a similar structure of a bright compact core with an east-west elongated structure.

The 12.5 μm image of NGC 2623 is shown in Figure 3a, along with the 8.4 GHz and NICMOS 2.2 μm images. The angular resolution of the 12.5 μm image is 0.7″, significantly lower resolution than either the 8.4 GHz (0.3″) or 2.2 μm (0.22″) images. The 12.5 μm image has been registered with respect to the radio and 2.2 μm images by assuming the peak brightness at 12.5 μm agrees with the peaks at the other wavelengths.

As can be seen from this figure, the structure of the 12.5 μm, 2.2 μm and 8.4 GHz images are all very similar and show similar sizes. The observed FWHM size of the 12.5 μm source is $1.0'' \times 0.7''$ or an intrinsic size of $0.7'' \times < 0.35''$ (260×<130 pc), with the major axis oriented east-west. The deconvolved size of the radio source is $0.43'' \times 0.29''$(160×110 pc). The overall extent of the 12.5 μm and 8.4 GHz emission agrees quite well, being $\sim 2'' \times 1.5''$ (740 × 550 pc) with the major axis oriented in the east-west direction. The excellent agreement between the 12.5 μm and 8.4 GHz maps of NGC 2623 is illustrated directly in Figure 3b, where the 12.5 μm contours are overlaid on the grayscale image of the 8.4 GHz image. The 2.2 μm NICMOS image shows a circular core with a size of 0.2″ (75 pc), and a larger nuclear region having the same size and orientation as that seen at 12.5 μm and 8.4 GHz.

The flux densities presented in Table 2, and fluxes shown in Figure 3c, show that the 12.5 μm flux density measured in a 4″ diameter beam represents 80% of the total flux density measured by IRAS at 12 μm, while 65% of the IRAS flux density is contained in a 1″ diameter beam. As in NGC 1614, the vast majority of the mid-infrared emission in NGC 2623 is confined to the nuclear region with a size of <400pc. The 8–13 μm spectrum presented by Dudley (1999) is consistent

with the observations reported here, and shows a PAH emission feature affecting the 11.7 μm flux measurement. The mid-infrared spectrum suggests significant silicate absorption of an underlying PAH emission spectrum, though quantifying this is highly uncertain.

4.4. NGC 3690+IC694=Arp 299=Mrk 171

NGC 3690+IC 694 (Arp 299, Markarian 171) is one of the most extensively studied interacting starburst galaxies known. Its optical morphology (Arp 1966) shows two main bodies with many bright internal knots and diffuse tidal debris extending over 90″ (20Kpc). This system was first shown to be a bright infrared and radio source by Gehrz, Sramek and Weedman (1983) who showed 10 μm emission extending over nearly 40″ (8 Kpc), encompassing both galactic nuclei. The redshift of NGC 3690 is cz=3120 Km/s (41 Mpc, 210 pc/″). IRAS measurements showed a total bolometric luminosity of $8\times10^{11}L_{\odot}$, making this the most luminous galaxy in this study (Soifer et al. 1987), and very close to the Ultraluminous Galaxy limit (Sanders et al. 1988).

The optical spectrum is classified as coming from a HII region (e.g., Villeux et al. 1995) while the mid-infrared spectrum of Dudley (1999) shows PAH emission and silicate absorption. Sargent and Scoville (1991) showed this system to be rich in molecular gas, while extensive near infrared studies have been reported by Sugai et al. (1999) and Satyapal et al. (1999) among others. A detailed near infrared study of NGC 3690 with NICMOS on HST has been reported by Alonso-Herrero et al. (2000a). Previous groundbased mid-infrared imaging of NGC 3690 has been reported by Miles et al. (1996) and Keto et al. (1997).

Figures 4a and 4b show the 12.5 μm image along with the NICMOS 2.2 μm, the 3.2 μm NIRC and the 8.4 GHz images of NGC 3690/IC694. The five nuclei identified at 2.2 μm are marked; the marks are reproduced at the same relative positions in all four panels of Figures 4a and 4b. We use here the nomenclature for the sources introduced by Gehrz, Sramek and Weedman (1983), and Wynn-Williams et al. (1991) of A, B1, B2, C and C′. Figure 4a shows the entire extent of the emission, while Figure 4b shows detailed maps of the western sources. The astrometric registration of the maps at different wavelengths is based on morphological similarities and direct measurements. The 8.4 GHz image of C91 and the 2.2 μm image of Alonso-Herrero et al. (2000a) were overlaid by assuming spatial coincidence of sources A and B1. The 2.2 μm and 3.2 μm images agree spatially to within 0.05″, based on NIRC measurements. After superposing the 12.5 μm image of source B1, at 12.5 μm the western sources (B1, B2, C and C') match the locations at 3.2 μm to <0.05″. Because of the extent of NGC 3690, the nod amplitude was increased to 20″, and all four sources of NGC 3690W were thus imaged on one frame at 12.5 μm and thus were registered accurately with respect to each other as seen in Figure 4b. NGC 3690 A was imaged separately at 12.5 μm, with no other objects in the field, and was registered with respect to the western cluster in Figure 1a by assuming its peak emission coincides with the 2.2 μm and 8.4Ghz peaks.

The emission seen at 12.5 μm is localized into five distinct emission centers at the locations of

A, B1, B2, C and C′. The total flux density from the sum of the individual components is reported in Table 2, and shows that the total flux density measured at 12 μm by IRAS is accounted for by the total of these components as measured in the groundbased observations. Thus at least at 12 μm there is negligible luminosity, in comparison to these sources, being emitted in the many other supergiant HII regions in this system. A similar conclusion has been reached by Alonso-Herrero et al. (2000a) based on the near infrared NICMOS observations of this galaxy.

A direct comparion between the 12.5 μm and 8.4 GHz maps of NGC 3690 is shown in Figure 4c, where the contours of the 12.5 μm image are overlaid on the grayscale of the 8.4 GHz image of C91. Sources B1, C and C' agree very well, while there is no apparent radio counterpart for the faint 12.5 μm source B2. The 12.5 μm sources are quite compact; the Keck data have a resolution of 0.6″ (125 pc), and only source C is clearly resolved in the Keck imaging.

While the vast majority of the infrared luminosity is produced by the five sources isolated at 12.5 μm, there is a low level of thermal infrared emission that is detected clearly in the 3.2 μm image. In Figure 4d the 3.2 μm image is stretched to show the low surface brightness emission, and for comparison the 1.644 μm [FeII] image from Alonso-Herrero et al (2000a). There is very low level 3.2 μm emission seen tracing the HII regions from source B2 to C, as well as the HII regions surrounding the nucleus in the eastern galaxy (Source A = IC694).

All of the sources detected at 12.5 μm are seen in the NICMOS 2.2 μm continuum images. The source C′ is inconspicuous in the near infrared image. This source has the largest ratio of $\frac{S_\nu(12\mu\ m)}{S_\nu(2.2\mu\ m)}$ of those detected at 12.5 μm, being more than 5 times brighter at 12.5 μm normalized to the 2.2 μm flux density than either sources A or B1, the brightest 12.5 μm sources. Alonso-Herrero et al (2000a) do not identify this as the source having the greatest extinction. This suggests that the more obscured sources (e.g. A, B1, C) have luminous stellar contributions associated with but separate from the highly infrared luminous regions.

Figures 4e and 4f show the spectral energy distributions of the various components. Figure 4e displays the SEDs of the integrated light from the entire system, the sum of 4″ diameter beams centered on A, B1, C and C', and a 2″ diameter beam centered on B2, and the individual SEDs in 2.5″ beams of the five separate peaks. Figure 4f presents three panels that show the SEDs of sources A, B and C separately in 1″ and 2.5″ diameter beams. The 2.2μm data are derived from NICMOS observations (Alonso-Herrero et al. (2000a), while the 3.2μm data are from NIRC observations shown in Figure 4d.

As mentioned above, the total flux density measured in the 12.5 μm images accounts for virtually all the flux density measured by IRAS (Soifer et al. 1989). The spectroscopy of Dudley (1999) shows that each of the separate sources, A, B1, C and C′ includes a contribution from PAH emission, while sources B1 and A also show overlying silicate absorption. The difficulty in determining the contribution of PAH emission to the photometry is illustrated by the comparison sources A and C in Figure 4d. Source A has an apparent small PAH contribution, but the spectrum of Dudley reveals that there is a substantial PAH emission feature superposed on a steeply rising

spectrum, while the similar strength feature seen in the SED of source C, which is suggestive of PAH emission in the photometry, is a result of being superimposed on a flatter SED for this source.

4.5. IC 883=UGC 8387=Arp 193

IC883=UGC 8387=Arp 193 is a disk galaxy with crossed tails in optical images suggestive of a merger. At a redshift of cz=7000 Km/s (92 Mpc, 470 pc/″), the infrared luminosity of this system is $3\times10^{11}L_{\odot}$ (Soifer et al. 1987). Its optical spectrum (Villeux, et al. 1995) is classified as that of a LINER, while its mid-infrared spectrum shows PAH emission (Dudley 1999). High resolution NICMOS observations of the bright central portion of this system reveal an apparently edge on disk galaxy with a significant dust lane (S00). High resolution radio observations show a source extended along the infrared disk with a size of $\sim 4'' \times 0.7''$ (C91).

Figure 5a shows the 12.5 μm Keck image, along with the 2.2 μm NICMOS image from S00 and the 8.4 GHz radio image from C91. The 12.5 μm image of Figure 5a is smoothed to 0.62″ resolution from the original 0.40″ to improve the signal-to-noise ratio, while the resolution is 0.19″ at 2.2 μm and 0.24″ at 8.4 GHz. Two peaks visible at 2.2 μm are marked; the marks are reproduced at the same relative positions in all three panels of Figure 5a.

The astrometric registration of the radio and 12.5 μm images is based on the assumption that the 12.5 μm peak coincides with the southeastern radio peak. This forces general agreement between the radio and 12.5 μm structures. The 2.2 μm image was registered with respect to the radio image by assuming coincidence of the central peak at 2.2 μm and the southeastern radio peak.

The 12.5 μm image shows that the emission is extended along a position angle of 135 °and shows a significant extension perpendicular to the major axis. The measured 12.5 μm FWHM is $1.8'' \times 0.7''$ while the full extent of the 12.5 μm emission is $3'' \times 1.7''$. The 8.4 GHz image shows a similar size along the major axis with significantly less extent perpendicular to this axis, having a full extent along the minor axis of 0.7″. With the assumption that the southeastern radio peak coincides with the peak of the 12.5 μm emission, the northwest radio peak appears to coincide with a shoulder of 12.5 μm emission. This is illustrated in Figure 5b where the 12.5 μm contours are overlaid on a grayscale of the 8.4 GHz image. The emission perpendicular to the major axis appears significantly more extended at 12.5 μm than at 8.4 GHz , but this could be a result of the lack of sensitivity to low surface brightness emission in the radio image.

The 2.2 μm image does not agree in morphology particularly well with the mid-infrared and radio images. Again we have assumed that the central peak of 2.2 μm emission coincides with the radio and infrared peaks, and present in Figure 5b a grayscale image of the NICMOS 2.2 μm image with 12.5 μm contours overlaid. The 2.2 μm peak to the northwest of the center differs in position relative to the radio peak by 0.2″ or 90 pc at the distance of the galaxy. In addition, the 2.2 μm extent is significant to the southeast of the central peak, while both the mid-infrared and 8.4 GHz

images show extent to the northwest of the central peak.

In addition to imaging IC 883 at 12.5 μm, Keck images were obtained at 8.0, 10.3 and 11.7 μm. These images showed virtually identical morphology to that shown in Figure 5a. Based on one dimensional profiles of flux vs. position from each Keck image there is no discernable variation in the SED of IC 883 along its major axis at a resolution of 0.6″ (270 pc) over the central 3″ or 1.4 Kpc. The spectral energy distribution of IC 883 is shown in Figure 5c. The comparison of the Keck observations and the IRAS data shows that the Keck observations account for all of the mid-infrared emission detected by IRAS in this system. The comparison of the 1″ and 4″ photometry illustrates the point that the SED does not vary significantly with beam diameter.

The Keck data show a strong drop in flux at 10 μm, indicative of significant silicate absorption affecting the emergent spectrum. The mid-infrared spectrum of Dudley (1999) shows strong PAH emission with a depression that is not nearly as strong as presented here. This apparent discrepancy is likely due to the low signal-to-noise ratio in the Dudley observations at ∼10 μm.

4.6. NGC 6090 = UGC 10267

NGC 6090 = UCG 10267, at a redshift cz = 8785 km/s (117 Mpc, 590 pc/″), has an infrared luminosity of $3\times10^{11}L_{\odot}$ (Soifer et al. 1987). The visual image shows a face-on spiral with a close companion separated by 5″ or ∼3 Kpc to the southwest and faint tidal tails extended over ∼ 2′ (72 Kpc). The optical spectrum is classified as HII like (Veilleux et al. 1995). High resolution VLA imaging at 8.4 GHz (C91) shows a compact source, while a lower resolution map at 1.4 GHz (Condon et al. 1990) shows emission extending over the face of both the spiral galaxy and the close companion. NICMOS observations have been reported for the NGC 6090 system by S00 and Dinshaw et al. (2000). Bryant and Scoville (1999) found that the molecular gas in this system is located approximately midway between the two galaxies.

The 12.5 μm image of NGC 6090 is presented in Figure 6a, along with the 2.2 μm image from S00, an 8.4 GHz image reprocessed from the data of C91 with angular resolution of 0.5″ and the Brγ image from Soifer et al. (2001). The astrometric registration of the radio and 12.5 μm images is based on the assumption that the brightest 12.5 μm peaks coincide with radio peaks with the same angular separation (and position angle). The mid-infrared image was located with respect to the near infrared continuum through the Brγ image. Because of the strong similarity in the morphological structure between the 12.5 μm and Brγ images, the 12.5 μm emission peaks were assumed to coincide with corresponding peaks in the Brγ image. The Brγ image was obtained using the Palomar Integral field Spectrograph (PIFS, Murphy et al. 1999) and was obtained simultaneously with a 2.2 μm continuum image of this galaxy. The 2.2 μm continuum image obtained with PIFS corresponds well with the 2.2 μm NICMOS image, so that the Brγ and 2.2 μm continuum images are located very precisely ($< 0.08''$) with respect to each other. The PIFS data will be discussed in more detail in Soifer et al.

In addition to the morphological similarities between the 12.5 μm and Brγ images there is a strong physical reason for expecting the emission to be spatially coincident; the currently ionzed gas traces the ionizing stars and the mid-infrared emission traces the dust heated by these (presumably) same stars.

With the *assumption* that the 12.5 μm and Brγ images coincide, a faint 12.5 μm peak to the east of the brightest regions in the image, coincides with the 2.2 μm nucleus in the face-on spiral NGC 6090. This is shown directly in Figure 6b, where the 12.5 μm contours are overlaid on a grayscale of the 2.2 μm image. The main emission at 12.5 μm coincides with regions of blue, unresolved sources in the spiral arms in the face-on spiral galaxy as noted by S00. In addition, the faint 12.5 μm emission $\sim 3''$ south and east of the bright 12.5 μm emission is located on a minor peak (not the bright point source) in the nearby companion galaxy. This region is spatially coincident with additional blue unresolved sources in the companion galaxy (S00). The bright unresolved source in the companion galaxy does not coincide with any radio or mid-infrared emission, consistent with the suggestion that it is a foreground object. The brightest mid-infrared peaks are extended by $\sim 1''$, or 600 pc, while the whole 12.5 μm emitting region in NGC 6090 is extended over $4'' \times 2''$, or 2.4 $\times$ 1.2 kpc.

With the astrometric registrations as presented in Figure 6a, the agreement between the peaks of 8.4 GHz emission and 12.5μm emission is quite good. Each peak of 12.5μm emission corresponds to a peak of radio emission (with perhaps a $0.2''$ discrepancy between the faint 12.5μm peak to the southeast and the corresponding radio peak). In addition, there appears to be a radio peak at the position of the near infrared nucleus of NGC 6090.

In NGC 6090 the galaxy nucleus is at best a minor source of infrared luminosity. The current location of luminous star formation appears to be in the spiral arms of the face-on galaxy and the portions of the companion galaxy closest to the spiral. These regions are within spiral arms and close to the molecular gas which lies between the two galaxies (Bryant and Scoville, 1999). This suggests that the molecular gas remained behind after the passage of the two galaxies on a closely interacting trajectory, and the current star formation was triggered in the locations of closest approach in the two galaxies.

Figure 6c shows the spectral energy distributions of the peaks in NGC 6090, along with the large beam IRAS and 2MASS data. At 12 μm approximately 50% of the flux density measured by IRAS is detected in the LWS images. The substantial difference between the 12 μm flux density measured by IRAS and the integrated flux density measured at 12.5 μm in the Keck image argues that there is significant diffuse mid-infrared emission in this system not detected in the ground-based imaging. Keck observations were obtained at 11.7, 12.5 and 17.9 μm. The increased flux density at 11.7 μm compared to that at 12.5 μm as seen in Figure 6c suggests that there is strong PAH emission in this system. There is no published spectrum of NGC 6090 spanning this wavelength range.

4.7. Markarian 331= UGC 12812

Markarian 331 = UCG 12812, at a redshift cz = 5500 km/s (73 Mpc, 370 pc/″), has an infrared luminosity of $2.5\times10^{11}L_{\odot}$ (Soifer et al. 1987). The visual image shows a high surface brightness core with no obvious tidal tails. There are two galaxies of comparable brightness located within 2′. The optical spectrum is classified as HII like (Veilleux et al. 1995), with a mid-infrared spectrum indicating a combination of PAH emission and silicate absorption (Dudley, 1999). High resolution VLA imaging at 8.4 GHz (C91) shows a bright central source surrounded by an elliptical ring of emission with dimensions 3″×2″.

Figure 7a shows the 12.5 μm image of Markarian 331 along with images at 2.15 μm (K_s), 3.4 μm and 8.4 GHz. A bright nucleus is seen at all wavelengths, as well as extended emission in an apparent disk or ring. In registering the images, it was assumed that the central peak was spatially coincident at all wavelengths.

At 8.4 GHz, the extended emission is distributed as a "ring" surrounding the bright nucleus. At 12.5 μm there is a bright nucleus that is unresolved in the 0.3″ seeing, as well as emission that appears to have a similar structure as the radio ring. The 12.5 μm emission appears to be distributed over the full disk of the system, extending over $\sim 4''$ or 1.5 Kpc diameter, with a "bar-like" structure extending from the nucleus to the northeast. The image of Markarian 331 obtained at 11.7 μm is virtually identical to that at 12.5 μm. At 8.4 GHz the emission is apparently confined to the nucleus and the ring. The latter effect may be a result of the very high resolution of the VLA image. The structure at 3.4 μm appears quite similar to that at 12.5 μm, showing a compact nucleus, a bar to the northeast and a disk. Figure 7b compares the images in the mid-infrared and radio directly, with an overlay of the 12.5 μm contours on a grayscale 8.4 GHz image. The structures are quite similar, with the peaks in the radio image corresponding very closely to the features in the mid-infrared image.

Figure 7c plots the fluxes in this system, comparing the mid-infrared flux densities to the IRAS and 2MASS measurements. The ground-based data account for >80% of the 12 μm flux density measured by IRAS, showing that the central ∼Kpc accounts for nearly all the infrared luminosity in this system. The similarity of the images at 11.7 and 12.5 μm shows that there is little evidence for variation in the spectral distribution of the infrared emission over the nuclear region. Roche et al. (1991) show that there is a strong PAH feature in the 10 μm spectrum of this galaxy, as well as strong silicate absorption.

5. Discussion

The galaxies observed in this study were selected to be highly luminous, active star forming galaxies that are bright in the 12 μm IRAS band. The mid-infrared observations reported here generally account for well more than half of the total 12 μm flux density as measured by IRAS.

This is seen in the figures of SEDs of the observed galaxies, where the observed mid-infrared fluxes are plotted with the IRAS fluxes. Only in NGC 6090 and VV114 is the 12.5 μm flux observed here less than half the IRAS 12 μm flux. In the remaining five systems, the the compact structures observed in the Keck images account for 80–100% of the total 12 μm flux density from the system. Thus our first conclusion is that star formation in these systems is not occuring over the entire disk of the galaxy, but is confined to relatively compact regions having sizes of $\sim$100 pc up to $\sim$ 1 Kpc.

The mid-infrared emission in these systems, as characterized by the 12.5 μm images presented in Figures 1–7, is far more compact than the overall distribution of near infrared light in these systems. This can be seen by comparing the 12.5 μm images of Figures 1a – 7a with the corresponding large field 2.2 μm NICMOS images from S00. The sizes of the mid-infrared sources are typically $\sim$ 0.3″ –2″, while the galaxy sizes seen in the NICMOS images (S00) are typically 10″–30″. The significantly smaller mid-infrared sizes compared to the near infrared sizes of these sources is shown directly in Figure 8, where we present the curves-of-growth of the 12.5 μm flux as a function of beam radius, compared to those at 2.2 μm and 1.1 (or 1.2) μm for the galaxies in the sample. The 12.5 μm flux vs. beam size was determined from the images in Figures 1a – 7a, with the normalization to 100% provided by the IRAS measured total flux density at 12 μm. The origin for the measurement beams was the location of peak 12.5 μm brightness as identified in the galaxy images of Figures 1a – 7a.

The corresponding curves-of-growth at 1.1 and 2.2 μm were determined from NICMOS images for VV114, NGC 2623, IC 883, NGC 6090 (from S00) NGC 1614 (from Alonso-Herrero et al. 2000b) and NGC 3690/ IC 694 (from Alonso-Herrero et al. 2000a) and from Palomar J and K_s imaging data for Markarian 331. The large beam normalizations for these data were based on the total J and K magnitudes of these galaxies as measured in the 2MASS database (T. Jarrett, private communication). For the 1.1 and 2.2 μm curves-of-growth, the origin for the measurement beams was the same as for the 12.5 μm beams, as shown in Figures 1a – 7a.

Figure 8 shows that for the galaxies where the ground-based 12.5 μm images account for the bulk of the total 12 μm flux of the galaxy, the radii of the regions producing 50% of the flux at 12.5 μm are <100 pc to $\sim$300 pc, while the equivalent radii at 1.2 and 2.2 μm are 1 to >2 Kpc. Noticeably different from this general characteristic are VV114 and NGC 6090, where a substantial fraction ($\sim$60%)of the 12 μm light is not detected in the ground-based observation, and is presumably extended, low surface brightness emission distributed over the galaxies. For both VV114E and NGC 6090 the curves-of-growth at 2.2 and 12.5 μm are quite similar.

The 2.2 μm light distribution is, in principle, relatively insensitive to dust extinction, although this is not the case for very dusty environments in the galaxies. To the extent that older stellar populations dominate the near infrared light in these galaxies, the 2.2 μm light traces the mass distribution of that population.

The 12 μm emission traces the current sites of luminous star formation. If the star forming regions within these galaxies are local examples of distant, dusty star forming galaxies, the global

SEDs of the distant star-forming galaxies would be more like those of the starburst regions within these galaxies, rather than like the SEDs of the whole galaxies, which have major contributions in the near infrared from stars not associated with the current starburst. The difference between the global SEDs and the SEDs of the star forming regions is illustrated quantitatively in the figures by the comparison of the integrated SEDs with the small aperture SEDs of the individual 12.5 μm sources in the galaxies. In all the galaxies, the SED of the individual star forming regions shows a significant increase in ratio of 12.5 μm to 2.2 μm flux in the small beams, compared to the integrated light of the galaxies. Typically this ratio is larger by a factor of two in the star forming region as compared to the integrated light for the galaxy, but it ranges to nearly an an order of magnitude for the reddest source (C$'$) in NGC 3690. For distant star forming galaxies, such as those seen in SCUBA submillimeter surveys (e.g. Eales et al. 2000), SIRTF observations will be required to obtain the equivalent observations to those presented here.

Presumably the 12.5 μm emission is tracing the far infrared emission associated with the same star formation complexes. If the fraction of the total infrared luminosity emitted by the individual regions in these galaxies is similar to the fraction of the 12.5 μm flux density compared to the total 12 μm flux density measured by IRAS, these regions produce from $\sim 10^{10} L_{\odot}$ to $\sim 4 \times 10^{11} L_{\odot}$ within a few hundred pc. While not as luminous as the ULIRGs, the star formation rates are still prodigious by comparison to normal galaxies like the Milky Way. The star formation rates are from 0.7 to 30 $M_{\odot}$/yr, based on the conservative luminosity/star formation rate conversion of Scoville and Young (1983) or Scoville and Soifer (1990). If the conversion from luminosity to star formation rate is a factor of several greater than this, as is the case for models that account for the formation of stars with mass <1 $M_{\odot}$(cf. Kennicutt, 1998), the total star formation rates go up accordingly.

Since the mid-infrared sources trace the high luminosity regions in these galaxies, these data provide direct evidence of the physical characteristics of the regions in which the starburst luminosity is being generated. Table 3 presents a summary of the sizes, brightness temperatures, and color temperatures of the mid-infrared sources. The inferred brightness temperature at 60 μm is calculated assuming the same angular size as measured at 12.5 μm, and assuming the same fraction of the total 60 μm flux density (as determined from the IRAS data) emerges from the region as is observed for the source at 12 μm. In physical sizes, the detected sources range from < 110 pc to almost 1 Kpc. In a few cases it is not physically possible for the bulk of the luminosity to emerge from sources of the sizes inferred from the 12.5 μm images, since the brightness temperature at 60 μm is larger than the color temperature of the source (here we assume that the color temperature is the global color temperature, determined from the IRAS 60 and 100 μm flux densities). In these cases the far infrared source size must be larger than the observed 12.5 μm source size. The minimum source sizes necesary for equal color and brightness temperatures at 60 μm are also given in Table 3, and generally are close to, or slightly larger than, the upper limits on sources sizes determined from the 12.5 μm Keck observations.

With these estimates of the physical sizes of the emitting regions determined, we can compare the derived surface brightnesses with those of both lower and higher luminosity sources. Table

3 includes the surface brightnessess in $L_\odot/Kpc^2$ derived from the FWHM estimated source sizes (corrected for the PSF size) and the fraction of the total luminosity of the source inferred from the 12.5 μm measured flux density for that source. As can be seen from Table 3, these values range from 2×10^{11} to $\sim 2\times10^{13} L_\odot/Kpc^2$. By comparison, the infrared surface brightnesses in the ULIRGs observed by Soifer et al. (2000) range from 1×10^{12} to $\sim 6\times10^{13}$ $L_\odot/Kpc^2$. In physical size, the starburst regions range from $\sim$ 120 pc (in VV114E$_{NE}$) to $\sim$ 1.2 Kpc (in Markarian 331), while the corresponding sizes of starburst regions in ULIRGs are quite similar, ranging from 140 pc in Arp 220 to 1.6 Kpc in IRAS 17208-0014. Thus, while the apparent physical sizes are similar to those found in ULIRGs, the apparent surface brightnesses of star formation are lower by factors of 3–10 or more. The difference in luminosities between the luminous starburst galaxies and the ULIRGS appears to be in the luminosity generated in a given volume rather than in the volume in which the luminosity is generated.

The core of Orion, with a luminosity of 2×10^5 $L_\odot$ over 0.3 pc (Werner et al. 1976), has an apparent surface brightness of 3×10^{12} $L_\odot/Kpc^2$, while the apparent face-on surface brightness of the starburst region in M82 is $\sim 2\times10^{11} L_\odot/$ Kpc^2 (Soifer et al. 2000). Previous work (Meuer et al. 1997) has shown that in normal galaxies, the surface brightness of star formation reaches an upper limit of $\sim 2\times10^{11} L_\odot/Kpc^2$ globally averaged over entire galaxies, with peak surface brightnesses of clusters of size $\sim$10 pc of $\sim 5\times10^{13} L_\odot/Kpc^2$. Thus the starburst regions in these systems appear extraordinary in comparison with normal galaxies, but not with respect to the highest density star forming environments within galaxies.

Table 4 summarizes the surface brightnesses of nearby starburst systems, the starburst regions in the galaxies in this sample, and the starburst regions in ULIRGs from Soifer et al. (2000). We can see clearly here that while there is significant scatter, there appears to be a natural progression in surface brightness in the galaxies, with increasing surface brightness accompanying increasing luminosity. Table 4 shows that in these luminous starburst galaxies environments equivalent to the core of Orion extend over hundreds of parsecs.

Turner, Beck & Ho (2000) and Gorjian, Turner & Beck (2001) have recently shown that in the nearby dwarf galaxy NGC 5253 star formation that produces $\sim 2\times10^9 L_\odot$ is occurring in a region $\sim$ 2 pc in size, i.e. in a "super starcluster". The observations described here cannot rule out the possibility that much of the luminosity in the starburst galaxies studied here emerges from regions of similar size, although the most luminous systems in this sample would require clusters of $\sim$100 such "super starclusters" in regions of order $\sim$200 pc in diameter.

In about half of the galaxies in this sample the luminosity appears to be generated in nuclear starbursts. In NGC 1614 and Markarian 331, a substantial fraction of the infrared luminosity is generated in a ring surrounding the nucleus. NGC 6090 presents the greatest exception to the nuclear starburst picture for high luminosity systems. Here the luminosity appears to be generated where the molecular gas remains from the recent interaction between the two galaxies. This might be the best example for a starburst triggered by cloud-cloud collisions in the galaxies disks.

The mid-infrared and radio emission generally trace each other quite well. Differences at the 100 pc scale are seen in VV114E$_{SW}$ and in the more extended emission in NGC 6090 and IC 883. It is most likely that the differences in the diffuse emission is a lack of sensitivity to low surface brightness emission in the 8.4 Ghz data.

6. Summary and Conclusions

We have obtained mid-infrared diffraction limited imaging of seven starburst galaxies with the Keck Telescopes. These observations have shown

1 - A substantial fraction, usually more than 50%, of the mid-infrared luminosity in these systems is generated in regions ranging in size from ∼100 pc to 1 Kpc,

2 - Nuclear starbursts generally dominate the starburst activity in these galaxies.

3 - In some cases, most notably NGC 6090, substantial infrared luminosity is generated in regions away from the galaxy nuclei, and is more likely associated with the region of physical interaction between two galaxies.

4 - The radio emission in starburst galaxies is a good tracer of the current location of compact star-formationing regions.

5 - Mid-infared emission is much more compact than is near infrared emission in these galaxies. If the starburst regions in these galaxies are prototypes for starforming galaxies at high redshift, the energy output of such galaxies should be dominated by the mid and far-infrared energy output more than is the case in the integrated light emerging from nearby starburst galaxies.

7. Acknowledgments

We thank J. Aycock, T. Stickel, G. Wirth, R. Campbell and Lee Armus for assistance with the observations. Barbara Jones, Rick Puetter and the Keck team brought the Long Wavelength Spectrograph (LWS) into service, enabling many of these observations. We thank Marcia Rieke and Susan Neff for providing data for NGC 3690, NGC 6090 and NGC 1614. Vassilis Charmandaris provided advice about ISO observations of VV 114. Joe Mazzarella provided us with data from NED, Tom Jarrett provided us with data from 2MASS, and Aaron Evans provided images from NICMOS. We also thank an anonymous referee for critical comments on this paper.

The W. M. Keck Observatory is operated as a scientific partnership between the California Institute of Technology, the University of California and the National Aeronautics and Space Administration. It was made possible by the generous financial support of the W. M. Keck Foundation. This research has made use of the NASA/IPAC Extragalactic Database which is operated by the Jet Propulsion Laboratory, Caltech under contract with NASA.

B.T.S, G.N., K.M. and E.E. are supported by grants from the NSF and NASA. B.T.S. and S.S are supported by the SIRTF Science Center at Caltech. SIRTF is carried out at the Jet Propulsion Laboratory. N.Z.S. was supported by NASA grant NAG5-3042. This work was carried out in part (M.R.) at the Jet Propulsion Laboratory, operated by the California Institute of Technology, under an agreement with NASA. The development of MIRLIN was suported by NASA's Office of Space Science. The National Radio Astronomy Observatory (J.J.C.) is a facility of the National Science Foundation operated under cooperative agreement by Associated Universities, Inc. This research has made use of the NASA/IPAC Extragalactic Database (NED), which is operated by the Jet Propulsion Laboratory, California Institute of Technology, under contract with NASA.

Fig. 1.—

Figure 1a A montage of contour plots is presented of the VV114E at 2.2 μm, 3.2 μm, 12.5 μm and 8.4 GHz. In this, and all subsequent figures, north is up and east to the left, and the FWHM size of the point spread function is shown separately in the panel for each wavelength as the hatched circle. In this, and all subsequent figures, contour levels are spaced by a factor of 1.34. The first contour is set to 90% of the peak brightness so that the third contour down represents 50% of the peak brightness. In this, and all subsequent figures, unless otherwise indicated the 2.2 $/mu$m images are from S00, while the radio images are from C91. In this, and all subsequent figures that display contour plots of the galaxies, the horizontal bar in one panel represents 500 pc at the galaxy. In Figure 1a the origin is chosen to be at the location of the northeast peak in the 2.2 μm image. The astrometric registration of the images at the different wavelengths is discussed in the text. The locations of the brightest peaks in the 2.2 μm image are indicated by a + and $\times$ in the same location in each panel.

Figure 1b A contour map of VV114E at 12.5 μm overlaid on the corresponding grayscale image of 8.4 GHz emission in the left panel. An overlay of the 3.2 μm emission contours on the corresponding grayscale image of 8.4 GHz emission is presented in the center panel. An overlay of the 12.5 μm emission contours on the corresponding grayscale image of the 2.2 μm emission is presented in the right panel. In these, and all subsequent gray scale images, the wavelength of the contoured image is given in the lower left corner and that of the gray scale image in the lower right.

Figure 1c A contour map of the full VV114 field at 3.2 μm overlaid on a gray scale image of the same region at 2.2 μm.

Figure 1d The spectral energy distributions for (top panel) all of VV114, VV114E, VV114E$_{NE}$ and VV114E$_{SW}$ and (bottom panel) all of VV114 repeated and VV114W. The data are plotted as flux per octave, νf_ν, vs. wavelength. In the top panel the integrated fluxes, taken from the IRAS and 2MASS data are shown as filled circles, along with photometry in a a 4$''$ diameter beam centered on VV114E (filled squares). In addition, photometry in 1$''$ diameter beams centered on VV114E$_{SW}$ ($\times$) and VV114E$_{NE}$(+) as indicated in figure 1a is also shown as open squares. In this, and all subsequent SEDs, the beam diameter for the photometry is indicated next to the identifying symbol. In this and the subsequent SEDs, the photometric points made with the same beam size are joined together with straight lines intended only to guide the eye. They are not intended to indicate the absence of significant structure between the data points presented, e.g., due to PAH emission or silicate absorption. The mid-infrared photometry is from data presented here. The 2.2 μm data are from the NICMOS imaging of S00, while the 3.2 μm data are from NIRC. In the bottom panel the integrated fluxes are repeated, as well as the measured emission for VV114W in a 4$''$ diameter beam centered on the western peak shown in Figure 1c.

Fig. 2.—

Figure 2a A montage of contour plots of NGC 1614 at Pα(1.87 μm), 2.2 μm, 12.5 μm, and

4.8 GHz is presented. The origin is chosen to be at the peak emission in the 2.2 μm image. The astrometric registration of the images at the different wavelengths is discussed in the text. The location of the center in each image is indicated by a + in each panel. The 2.2 μm broadband and the 1.87 μm Pα NICMOS images are from Alonso-Herrero et al. (2000b).

Figure 2b A contour map of NGC 1614 at 12.5 μm is overlaid on the corresponding grayscale image of Pα emission in the left panel. An overlay of the 12.5 μm emission contours on the corresponding grayscale image of 4.8 GHz emission is presented in the right panel.

Figure 2c The spectral energy distribution of NGC 1614 is shown. The filled circles represent the integrated fluxes taken from IRAS and 2MASS data. The aperture photometry in a 4″ diameter beam is represented by filled squares, the photometry in a 2″ diamater beam is represented by open circles. The 2″ diameter was set to include the ring of emission seen in Figure 2b. The 2.2 μm photometric data are from the NICMOS image on NGC 1614 (Alonso-Herrero et al., 2000b) and Carico et al. (1988).

Fig. 3.—

Figure 3a A montage of contour plots is presented of NGC 2623 at 2.2 μm, 12.5 μm, and 8.4 GHz. The origin is chosen to be at the peak emission in the 2.2 μm image. The astrometric registration of the images at the different wavelengths is discussed in the text. The location of the center in each image is indicated by a + in each panel.

Figure 3b A contour map of NGC 2623 at 12.5 μm is overlaid on the corresponding grayscale image of 8.4 GHz emission.

Figure 3c The spectral energy distribution of NGC 2623 is shown. The filled circles represent the integrated fluxes taken from IRAS and 2MASS data. The aperture photometry in a 4″ diameter beam is represented by filled squares, the photometry in a 1″ diamater beam is represented by open circles. The 2.2μm photometric data are scaled from (S00).

Fig. 4.—

Figure 4a A montage of contour plots is presented of NGC 3690/IC 694 at 2.2 μm, 3.2 μm, 12.5 μm and 8.4 GHz. The positions of sources A, B1, B2, C and C′ as determined at 2.2 μm are indicated in each panel. The astrometric registration of the images at the different wavelengths is discussed in the text. The 2.2 μm image is from Alonso-Herrero et al. (2000a) and the 3.2 μm image is from NIRC.

Figure 4b A montage of contour plots of NGC 3690 at 2.2 μm, 3.2 μm, 12.5 μm and 8.4 GHz is given. This is an expanded scale of the western portion of Figure 4a, showing in more detail the sources in NGC 3690, but otherwise the same as in Figure 4a.

Figure 4c A contour map of NGC 3690 at 12.5 μm overlaid on the corresponding grayscale image of 8.4 GHz emission is shown.

Figure 4d Grayscale images of NGC 3690/IC 694 at 3.2 μm and in the [FeII] 1.644 μm emission line + continuum (from Alonso-Herrero et al. 2000a) are shown. Both images has been stretched to enhance the low level emission.

Figure 4e The spectral energy distributions of sources in NGC 3690 / IC 694 are presented. The integrated fluxes are represented by filled circles, and are taken from IRAS and 2MASS data. The filled squares represent photometry in a 2.5″ diameter beam centered on sources A, B1, C and C′ and a 2″ diameter beam centered on source B2 as shown in Figures 4a and 4b. The filled triangles represent the sum of the photometric points for the individual sources using a 4″ beam for sources A, B1, C, and C′ and a 2″ beam for B2. The 3.2 μm data are from NIRC, while the 2.2 μm data for the small beams are from NICMOS (Alonso-Herrero et al. 2000a).

Figure 4f The spectral energy distributions of individual sources in NGC 3690 / IC 694. The filled triangles represent the sum of all the photometric points for the individual sources, and are presented for reference in each panel. In the top panel are data for source A in 1″ (filled squares) and 2.5″ (open squares) diameter beams. The middle panel presents data for sources B1 (1″diameter beam - open squares, 2.5″diameter beam - filled squares) and B2 (1″diameter beam - open squares, 2″diameter beam - filled stars). The bottom panel presents data for sources C (1″diameter beam - open squares, 2.5″diameter beam - filled squares) and C′ (1″diameter beam - open squares, 2.5″diameter beam - filled squares). The data sources are as in Figure 4e.

Fig. 5.—

Figure 5a A montage of contour plots is presented of IC 883 at 2.2 μm, 12.5 μm and 8.4 GHz. The origin is chosen to be at the peak emission in the 2.2 μm image. The astrometric registration of the images at the different wavelengths is discussed in the text. The location of the two brightest peaks at 2.2 μm are indicated in each image by a + and $*$ at the same relative location in each panel.

Figure 5b An overlay of the 12.5 μm emission contours of IC 883 on the corresponding grayscale image at 2.2 μm is presented in the left panel. A contour map at 12.5 μm is overlaid on the corresponding grayscale image of 8.4 GHz emission in the right panel.

Figure 5c The spectral energy distribution of IC 883 is shown. The filled circles represent the integrated fluxes taken from IRAS and 2MASS data. The aperture photometry in a 4″ diameter beam is represented by filled squares, the photometry in a 1″ diamater beam is represented by open circles. The 2.2 μm photometric data are scaled from the NICMOS image (S00).

Fig. 6.—

Figure 6a A montage of contour plots is presented of NGC 6090 at Brγ (2.16 μm), 2.2 μm, 12.5 μm, and 8.4 GHz. The origin is chosen to be at the nucleus of the face-on spiral galaxy in the 2.2 μm image, and is indicated by a + in each panel. The astrometric registration of the images at the different wavelengths is discussed in the text. The location of a secondary peak at 2.2 μm

is indicated by a $*$ in each panel. The location of the secondary peak in the 8.4 GHz emission is indicated by a $\times$ in each panel. The Brγ image was obtained using the Palomar Integral field Spectrograph (PIFS, Murphy et al. 1999).

Figure 6b A contour map of NGC 6090 at 12.5 μm is overlaid on the corresponding grayscale image at 2.2 μm (left) and 8.4 GHz image (right).

Figure 6c The spectral energy distributions of the sources in NGC 6090 are shown. The filled circles represent the integrated fluxes taken from IRAS and 2MASS data. The filled squares represent photometry in a $6''$ diameter beam centered on the eastern source. The open squares and open triangles represent photometry in a $1.5''$ diameter beam centered on the southern and northern components of the eastern source. The open circles and filled squares marked with a W present photometry in $1.5''$ and $4''$ diameter beams centered on the western source. The 2.2 μm photometric data are scaled from the NICMOS image (S00).

Fig. 7.—

Figure 7a A montage of contour plots is presented of Markarian 331 at 2.15 μm, 3.4 μm, 12.5 μm and 8.4 GHz. The origin is chosen to be at the bright nucleus in each panel and is indicated by a $+$ in each panel. The 2.15 μm and 3.4 μm images are from the 200-inch Hale Telescope.

Figure 7b A contour map of Markarian 331 at 12.5 μm is overlaid on the corresponding grayscale image of 8.4 GHz emission.

Figure 7c The spectral energy distribution of sources in Markarian 331 are shown. The filled circles represent the integrated fluxes taken from IRAS and 2MASS data. The aperture photometry in a $4''$ diameter beam is represented by filled squares, the photometry in a $1.5''$ diamater beam centered on the nucleus is represented by open circles. The photometry in the annulus between the $1.5''$ diamater and $4''$ diameter is shown as open squares.

Fig. 8.—

A montage of the normalized curves-of-growth (included flux density vs. beam size) is shown for the galaxies in this sample at 12.5 μm (solid line), 2.2 μm (dashed line) and 1.1 μm (or 1.2 μm in the case of Markarian 331, dotted line). The normalization to 1.0 is taken from the IRAS 12 μm flux density for the 12.5 μm curve and the integrated magnitudes of these galaxies at 2.2 and 1.2 μm from the 2MASS all sky survey (Jarrett, private communication). The physical scale for each galaxy was taken from the data in Table 1. No correction has been applied for the PSF size, so that in some cases, e.g., NGC 3690 A and B and NGC 2623, the profile reflects the curve of growth of the PSF. In all cases the centers of the beams for the curves-of-growth are at the peak surface brightness at 12.5 μm as shown in figures 1a – 7a. The same location is taken for the center of the beams at all wavelengths. In the case of NGC 3690 the center location of NGC 3690 B is taken as the location of source B1. The effects of the $4''$ chopping amplitude are seen in the 12.5 μm curves for NGC 1614, NGC 2623, and IC 883.

REFERENCES

Alonso–Herrero, A., Rieke, G.H., Rieke, M.J. and Scoville, N.Z. 2000a, ApJ, 532, 845

Alonso–Herrero, A., Engelbracht, C.W., Rieke, M.J., Rieke, G.H. and Quillen, A.C. 2000b, astro-ph 0008317

Arp, H. 1966, ApJS, 14, 1

Beichman, C.A., Neugebauer, G., Habing, H.J., Clegg, P.E. and Chester, T.J. eds.1989, Infared Astronomical Satellite (IRAS) Catalog and Atlases, Explanatory Supplement, 2nd Edition, Washington DC, US Government Printing Office

Carico, D.P., Sanders, D.B., Soifer, B.T., Elias, J.H.,

Condon, J. J., Helou, G., Sanders, D.B. and Soifer, B.T. 1990, ApJS, 73, 359

Condon, J. J., Huang, Z. P., Yin, Q. F., Thuan, T. X., 1991, ApJ, 378, 65(C91)

Dale, D.A., Helou, G., Contursi, A., Silbermann, N.A. and Sonali, K.2000, astro-ph 0011014

Doyon, R., Nadeau, D, Joseph, R.D., Goldader, J.D., Sanders, D.B. and Rowlands, N. 1995, ApJ, 450, 111

Dinshaw, N. Evans, A.S., Epps, H., Scoville, N.Z. and Rieke, M.J. 1999, ApJ, 525, 702

Dudley, C.C., 1999, MNRAS, 307, 553

Frayer, D.T., Ivison, R.J., Smail, I., Yun, M.S. and Armus, L. 1999, AJ, 118, 139

Gehrz, R.D., Sramek, R.A. and Weedman, D.W. 1983, ApJ, 267, 551

Gorjian, V., Turner, J.L. and Beck, S.C. 2001, astro-ph 0103101

Harper, D.A. and Low, F.J. 1973, ApJ, 182, L89

Hauser, M.G. et al. 1998, ApJ, 508, 25

Jones, B. and Puetter, R.C. 1993, Proc. SPIE, 1946, 610

Keto, E. et al. 1997, ApJ, 485, 598

Kennicutt, R.C. 1998, ApJ, 498, 541

Kim, D.-C., Sanders, D.B., Veilleux, S., Mazzarella, J.M. and Soifer, B.T. 1995, ApJS, 98, 129

Kleinmann, D.E. and Low, F.J. 1970, ApJ, 161, L203

Knop, R.A., Soifer, B.T., Graham, J.R., Matthews, K., Sanders, D.B.and Scoville, N.Z. 1994, AJ, 107, 920

Laurent, O., Mirabel, I.F., Charmandaris, V., Gallais, P., Madden, S.C., Sauvage, M., Vigroux, L. and Cesarsky, C. 2000, A&A, 359, 887

Li, A. and Draine, B.T. 2000, astro-ph 0011319

Matthews, K. and Soifer, B.T. 1994, *Infrared Astronomy with Arrays: the Next Generation*, I. McLean ed. (Dordrecht: Kluwer Academic Pub.), P.239

Meurer, G.R., Heckman, T.M., Lehnert, M.D., Leitherer, C. and Lowenthal, J. 1997, AJ, 114, 54

Miles, J. W., Houck, J. R., Hayward, T. L., Ashby, M. L. N., 1996, ApJ, 465, 191

Murphy, T.W, Soifer, B.T., Matthews, K. 1999, PASP, 111, 1176

Neff, S.G., Hutchings, J.B., Stanford, S.A. and Unger, S.W. 1990, AJ, 99, 1088

Persson, S.E., Murphy, D.C., Krzeminski, W., Roth, M. and Rieke, M.J. 1998, AJ, 116, 2475

Puget, J.L., Abergel, A., Bernard, J.P., Boulanger, F., Desert, F.X. and Hartmann, D. 1996, A&A, 308, L5

Ressler, M. E.,Werner, M. W., Van Cleve, J. and Choa, H., 1994, Experimental Astronomy, 3, 277

Rieke, G.H. and Low, F.J. 1972, ApJ, 176, L95

Roche, P.F., Aitken, D.K., Smith, C.H. and Ward, M.J., 1991,MNRAS, 248, 606

Sanders, D.B. and Mirabel, I.F. 1996, Ann. Rev. Astron & Astrophys., 34, 749

Sanders, D.B., Soifer, B.T., Elias, J.H., Madore, B.F., Matthews, K., Neugebauser, G. and Scoville, N.Z. 1988, ApJ, 325, 74

Sargent, A.I. and Scoville, N.Z. 1991, ApJ, 366, L1

Satyapal, S., Watson, D.M., Forrest, W.J., Pipher, J.L., Fischer, J, Greenhouse, M.A., Smith, H.A. and Woodward, C.E. 1999, ApJ, 516, 704

Scoville, N.Z.and Young, J.S. 1983, ApJ, 265, 148

Scoville, N.Z. and Soifer, B.T. 1990, *Massive Stars in Starbursts* ed. C. Leitherer, N. Walborn, T. Heckman and C. Norman (Cambridge: Cambridge Univ. Press) P. 233

Scoville, N. Z., Evans, A. S., Thompson, R., Rieke, M., Hines, D.C., Low, F.J., Dinshaw, N., Surace, J.A. and Armus, L.. S00, 2000, AJ, 119, 991

Soifer, B. T., Boehmer, L., Neugebauer, G. and Sanders, D.B. 1989, AJ, 98, 766

Soifer, B. T., Neugebauer, G., Matthews, K., Egami, E., Becklin, E.E., Weinberger, A.J., Ressler, M., Werner, M.W., Evans, A.S., Scoville, N.Z., Surace, J.A., and Condon, J.J. 2000, AJ, 119, 509

Soifer, B. T. et al. 2001, in preparation

Soifer, B. T., Sanders, D. B., Madore, B. F., Neugebauer, G., Danielson, G. E., Elias, J. H., Lonsdale, C. J., and Rice, W. L., 1987, ApJ, 320, 238

Sugai, H, Davies, R.I., Malkan, M.A., McLean, I.S., Usuda, T. and Ward, M.J. 1999, ApJ, 527, 778

Turner, J.L., Beck, S.C. and Ho, P.T.P. 2000, ApJ, L109

Veilleux, S., Kim, D.-C., Sanders, D.B., Mazzarella, J.M. and Soifer, B.T. 1995, ApJS, 98, 171

Veilleux, S., Sanders, D.B., and Kim, D.-C. 1999, ApJ, 522, 139

Wynn-Williams, C.G., Eales, S.A., Becklin, E.E., Hodapp, K.-W., Joseph, R.D., McLean, I.S., Simons, D.A. and Wright, G.S. 1991, ApJ, 377, 426

Werner, M.W., Gatley, I., Becklin, E.E., Harper, D.A., Loewenstein, R.F., Telesco, C.M. and Thronson, H.A. 1976, ApJ, 204, 402

Yun, M.S., Scoville, N.Z. and Knop, R.A. 1994, ApJ, 430, L109

Table 1

Table 1: Basic Properties of Observed Galaxies

Name	z	log L $L_{bol}[L_\odot]$	logM_{H_2} $[M_\odot]$	Spectrum opt/ir	linear scale pc/″
VV 114 = Arp 236	0.0200	11.62	10.44	HII/PAH	400
NGC 1614 = Arp 186	0.0159	11.62	10.03	HII/...	320
NGC 2623 = Arp 243	0.0185	11.54	9.77	..../PAH	370
NGC 3690/IC694 = Arp 299	0.0104	11.91	10.06	HII/PAH+Sil	210
IC 883 = Arp 193	0.0233	11.51	9.87	LINER/PAH	470
NGC 6090 = Mrk 496	0.0293	11.51	10.15	HII/...	590
UGC 12812 = Mrk 331	0.0185	11.41	10.11	HII/PAH+Sil	370

Table 2

Table 2: Keck Mid-Infrared Flux Densities for Starburst Galaxies[a]

Object	7.9μm [mJy]	8.8μm [mJy]	9.7μm [mJy]	10.3 μm [mJy]	11.7μm [mJy]	12.5μm [mJy]	12μm[b] [mJy]	17.9μm [mJy]
VV114E	457	245	52±21	70±10	237	338	1100	452±61
NGC 1614[c]	···	···	···	···	1030	1220	1400	···
NGC 2623	···	···	···	···	151	201	240	···
NGC 3690 sum[d]	···	···	···	···	2390	4030	3900	12650
IC 883	335±34	···	···	34±11	130	301±46	260	···
NGC 6090 sum[e]	···	···	···	···	167	134	290	356±40
Mrk 331	···	···	···	···	280	403	510	685

[a]The Keck flux densities are in a 4″ diameter circular beam unless otherwise noted. The uncertainties are omitted from the table unless the statistical uncertainty in the photometry, based on the noise in the sky, exceeds 10%. The uncertainties quoted are statistical only; photometric uncertainties are on the order of ±10%.

[b]The 12 μm flux densities are from the IRAS data for these objects. The effective beam size is 2′ for the IRAS measurements. The uncertainties in the IRAS data are 5-10%.

[c]At 24.5 μm a flux density of 7.0 Jy was measured

[d]The flux densities are the sum of the flux densities measured in four separate 4″ diameter beams centered on NGC 3690 A, NGC 3690 B1, NGC 3690 C, and NGC 3690 C′, and a 2″ diameter circular beam centered at NGC 3690 B2.

[e]The flux densities in a 6″ diameter beam centered on NGC 6090E$_S$ and a 4″ beam centered on NGC 6090W

Table 3

Table 3: Sizes and surface brightnesses in Starburst Galaxies

Object	size of mid-ir source		$\frac{f_{12.5\mu m}(Keck)}{f_{12\mu m}(IRAS)}$	$T_b(12\mu m)$	$T_b(60\mu m)$	$T_c(60\mu m)$	$L_{ir}[L_\odot]$	$\frac{L}{A}[L_\odot Kpc^{-2}]$
	$''$	pc		K	K	K		
VV114E sw	0.37	150	0.30	94	57	54	1.2×10^{11}	
	> 0.41	> 165	0.30	92	54	54	1.2×10^{11}	$< 5.6 \times 10^{12}$
VV114E ne	0.29	120	0.12	91	51	54	5.0×10^{10}	4×10^{12}
NGC 1614	1.70	550	0.87	84	41	62	3.6×10^{11}	1.5×10^{12}
NGC 2623	$0.7\times < 0.3$	$260\times < 110$	0.85	>89	>65	64	3.0×10^{11}	
	> 0.52	> 192	0.85	88	64	64	3.0×10^{11}	$< 1.0 \times 10^{13}$
NGC 3690 A	< 0.60	< 125	0.32	>100	69	66	2.6×10^{11}	
	> 0.65	> 137	0.32	98	66	66	2.6×10^{11}	$< 1.8 \times 10^{13}$
NGC 3690 C′	< 0.60	< 125	0.04	>85	>44	66	3.2×10^{10}	$> 2.6 \times 10^{12}$
NGC 3690 C	1.1	230	0.12	79	42	66	1.0×10^{11}	2.4×10^{12}
NGC 3690 B1	< 0.60	< 125	0.51	>104	>80	66	4.0×10^{11}	
	> 0.84	> 176	0.51	98	66	66	4.0×10^{11}	$< 1.6 \times 10^{13}$
NGC 3690 B2	< 0.6	< 125	0.015	>78	>37	66	1.2×10^{10}	$> 1.0 \times 10^{12}$
IC 883	1.5×0.4	700×190	1.00	84	20	46	3.2×10^{11}	2.0×10^{12}
NGC 6090E S	1.5×1.0	890×590	0.30	73	30	51	9.7×10^{10}	2.4×10^{11}
NGC 6090E N	1.0	590	0.12	71	28	51	3.9×10^{10}	1.4×10^{11}
NGC 6090W	<0.6	<350	0.04	71	>29	51	1.3×10^{10}	$> 1.3 \times 10^{11}$
Mrk 331 n	(<0.6)	<225	0.2	>81	>41	58	5×10^{10}	$> 1.3 \times 10^{12}$
Mrk 331 r	4×2.7	1500×1000	0.63	71	30	58	1.6×10^{11}	1.4×10^{11}

Table 4: **Surface Brightnesses of Infrared Starburst Galaxies**

Object	Type	Infrared Luminosity $L_{bol}[L_\odot]$	Surface Brightness $[L_\odot Kpc^{-2}]$
ORION	HII Region	1×10^{6}	2×10^{12}
M 82	Local Starburst	3×10^{10}	2×10^{11}
NGC 6090	Starburst	3×10^{11}	2×10^{11}
NGC 1614	Starburst	4×10^{11}	1.5×10^{12}
Mrk 331	Starburst	2.5×10^{11}	$\sim 2 \times 10^{12}$
IC 883	Starburst	3×10^{11}	2×10^{12}
VV 114	Starburst	4×10^{11}	$\sim 5 \times 10^{12}$
NGC 2623	Starburst	3×10^{11}	$\sim 10^{13}$
NGC 3690	Starburst	8×10^{11}	$\sim 10^{13}$
IRAS17208	ULIRG	3×10^{12}	1.2×10^{12}
Mrk 273	ULIRG	1.3×10^{12}	$> 2.2 \times 10^{13}$
IRAS08572	ULIRG	1.3×10^{12}	$> 2.8 \times 10^{13}$
Arp 220	ULIRG	1.5×10^{12}	6.0×10^{13}

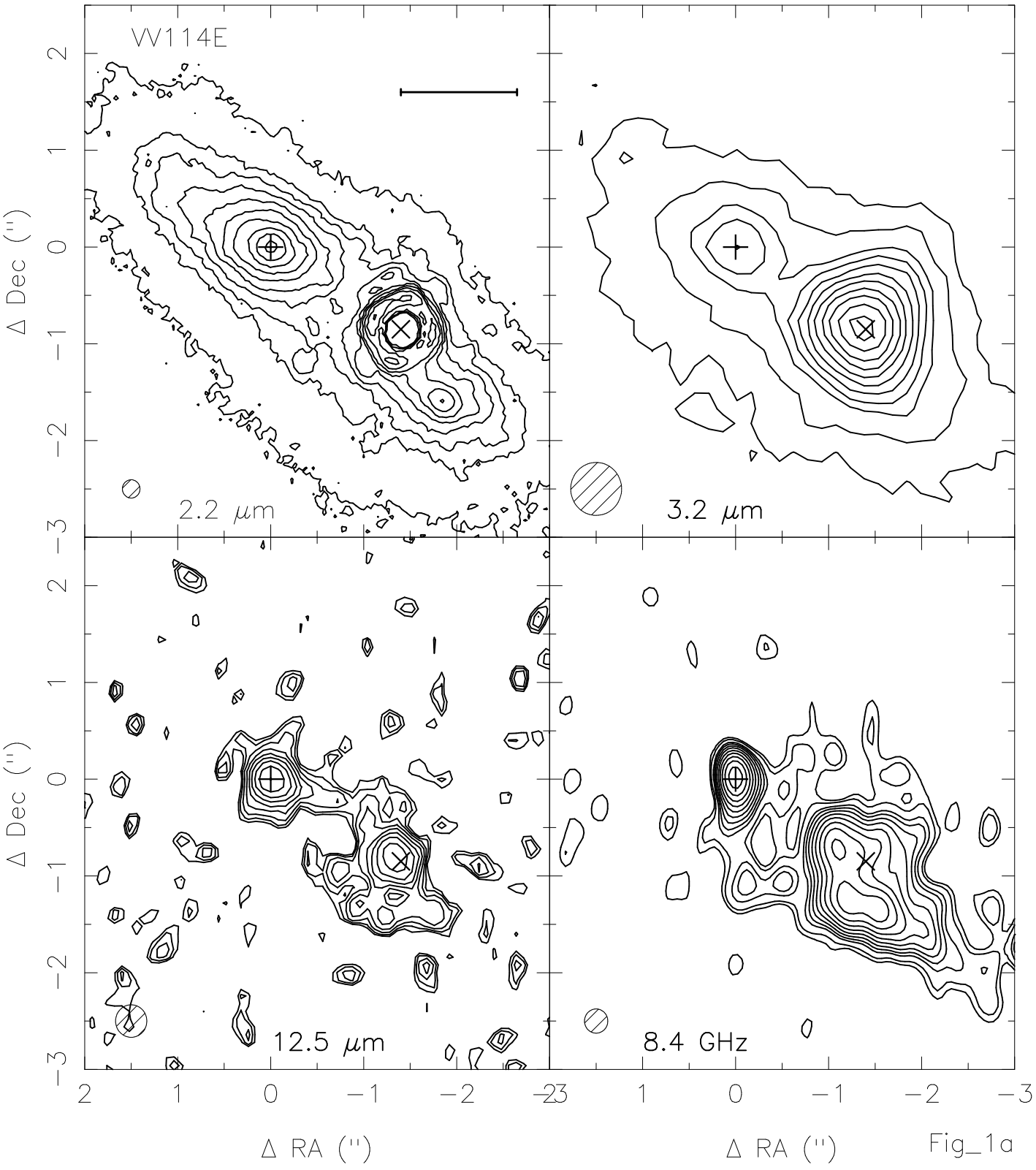

Fig_1a

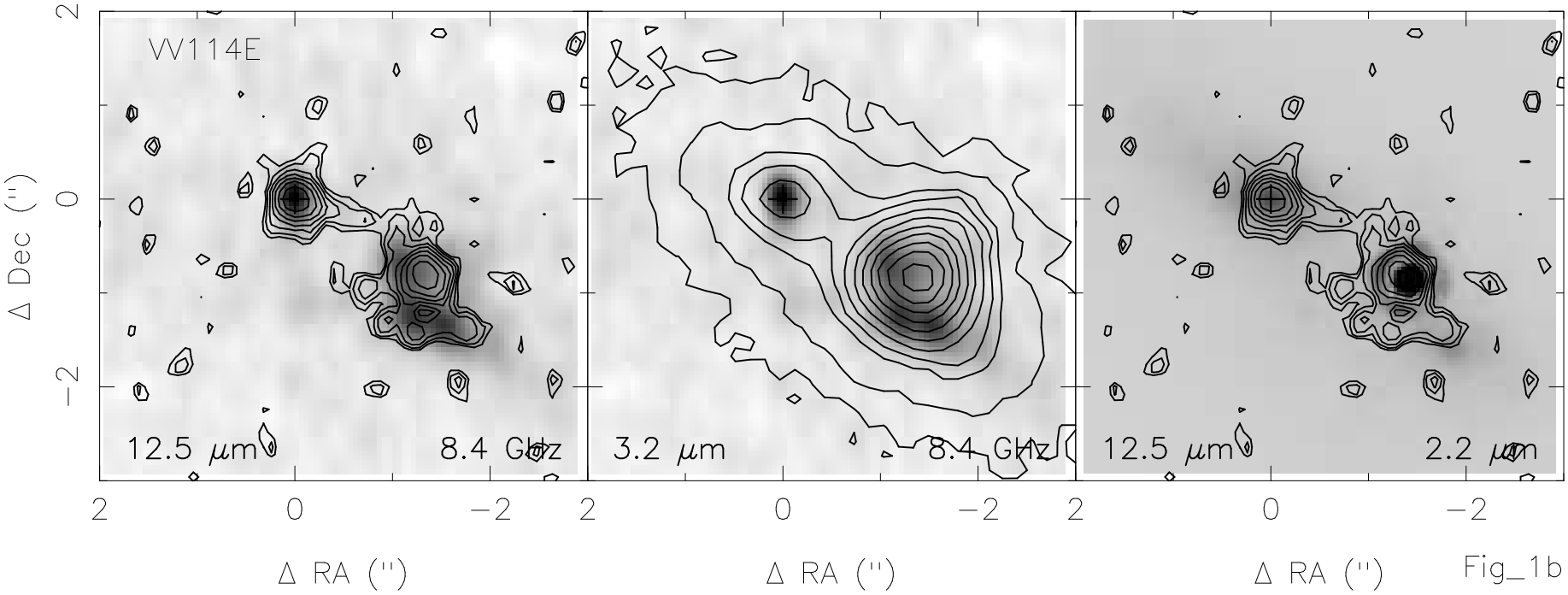
VV114E
12.5 μm
8.4 GHz
3.2 μm
8.4 GHz
12.5 μm
2.2 μm
Δ Dec (")
Δ RA (")
Δ RA (")
Δ RA (")
2
0
−2

Fig_1b

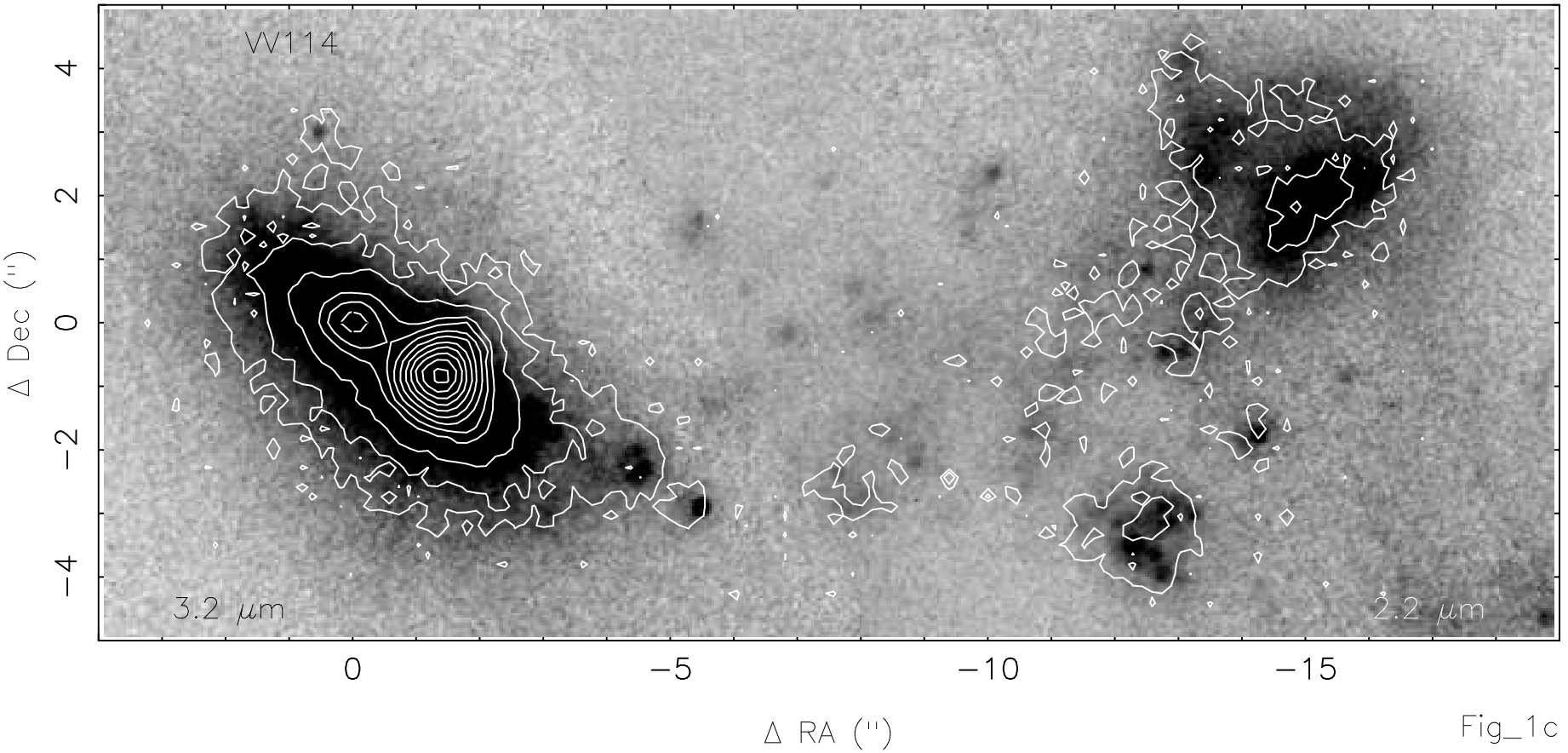

Fig_1c

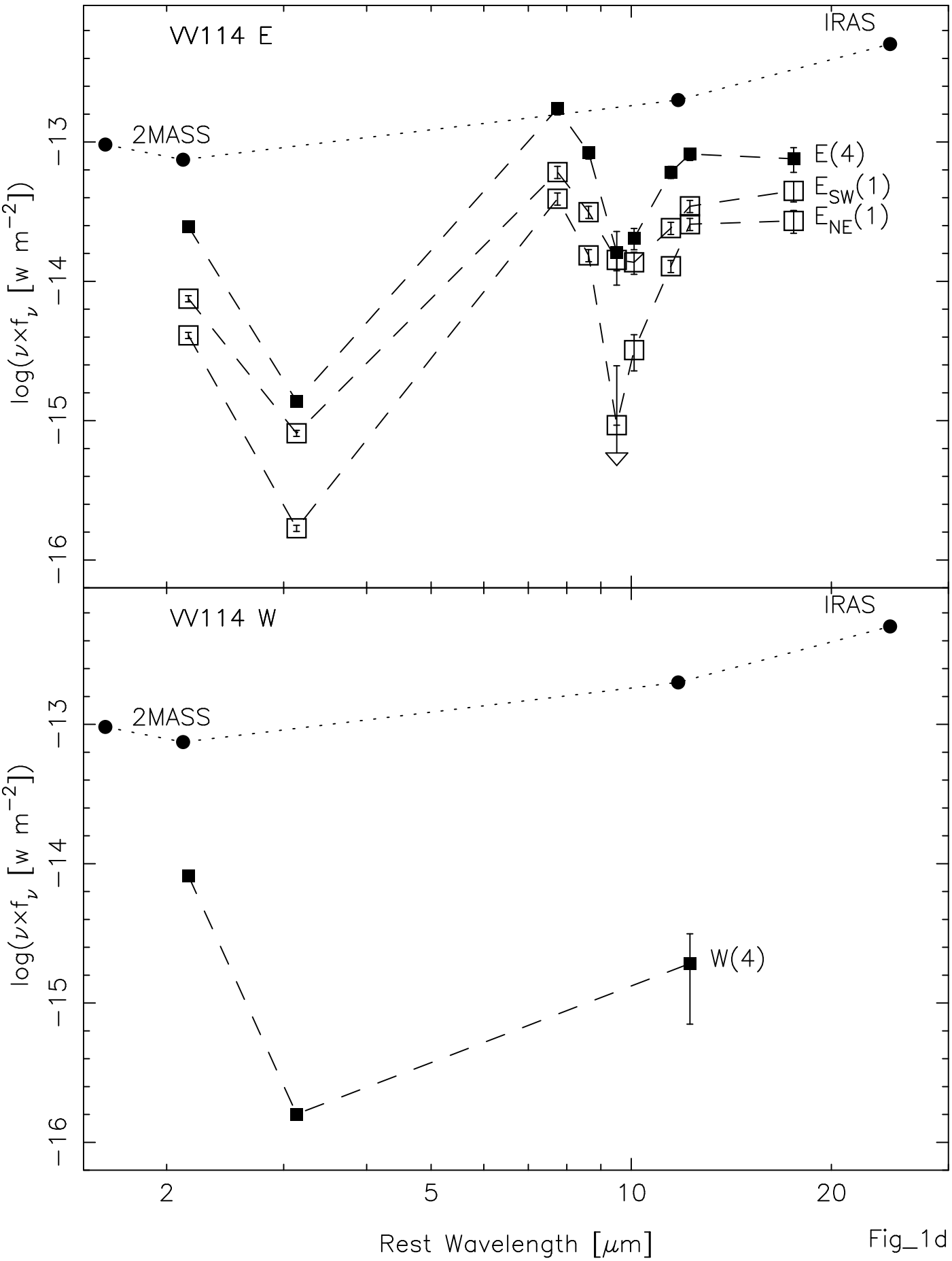
W114 E
IRAS
2MASS
E(4)
$E_{SW}(1)$
$E_{NE}(1)$
W114 W
IRAS
2MASS
W(4)
$\log(\nu \times f_\nu\ [w\ m^{-2}])$
−13
−14
−15
−16
2
5
10
20
Rest Wavelength [μm]

Fig_1d

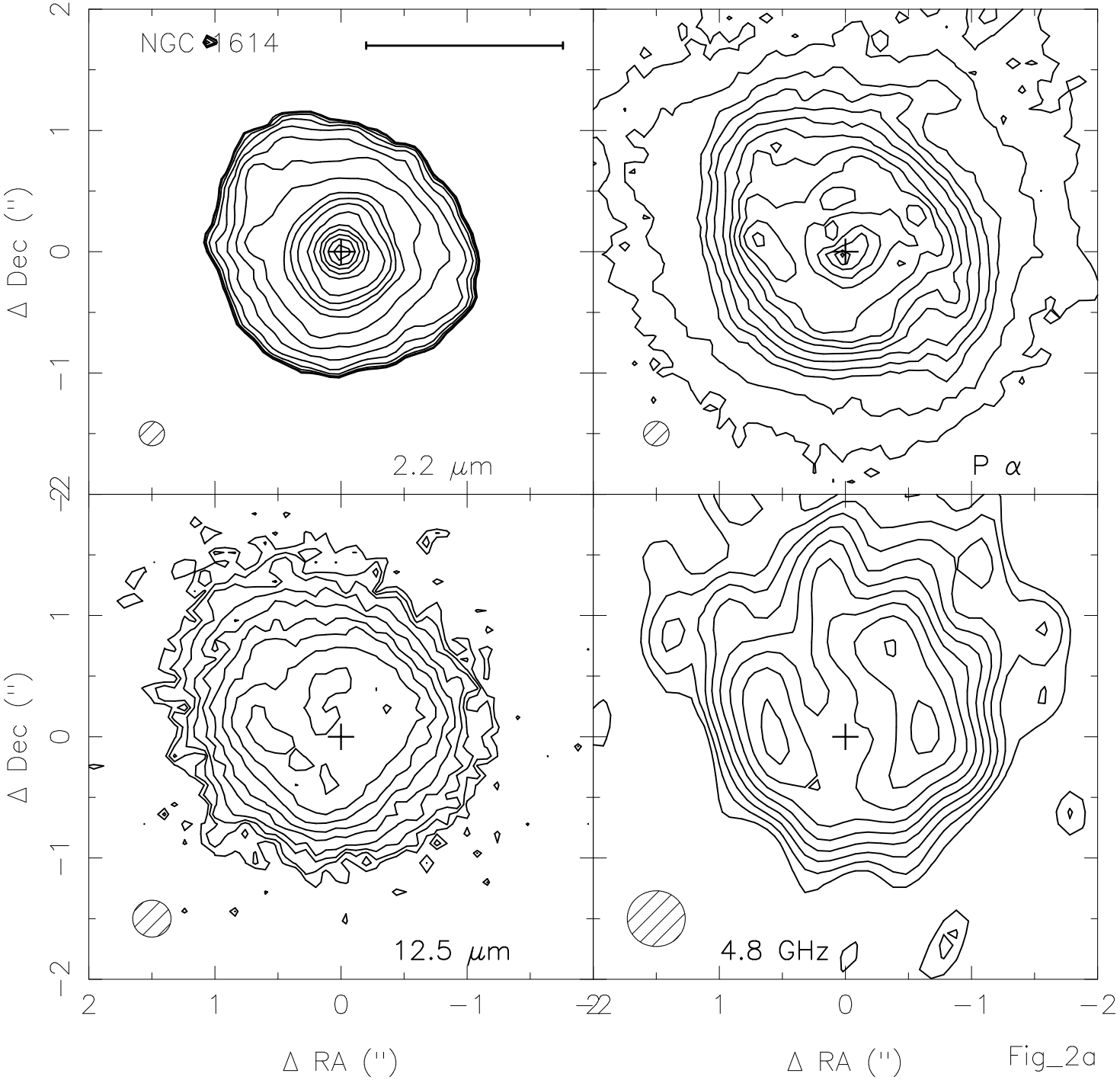

Fig_2a

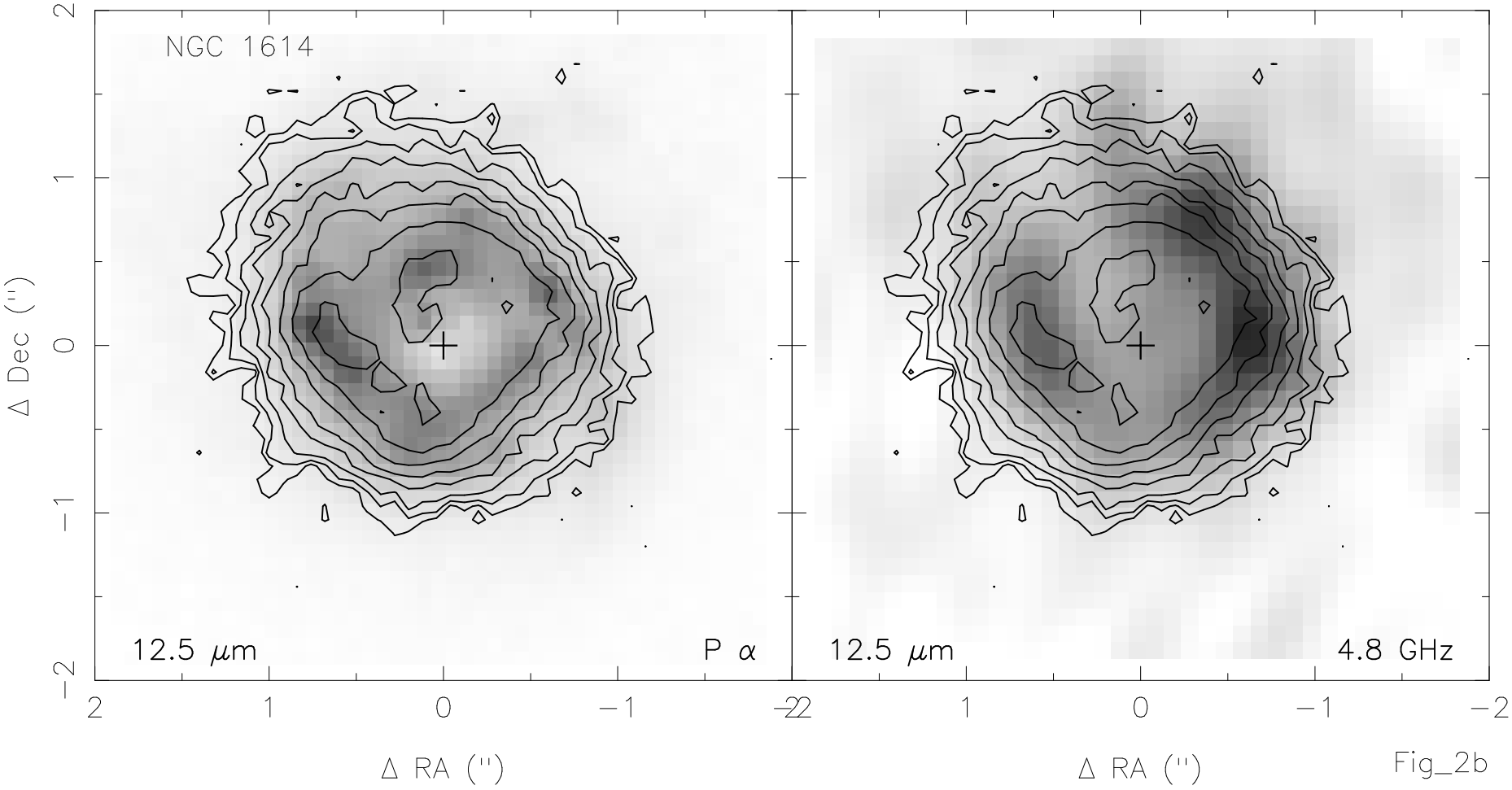

Fig_2b

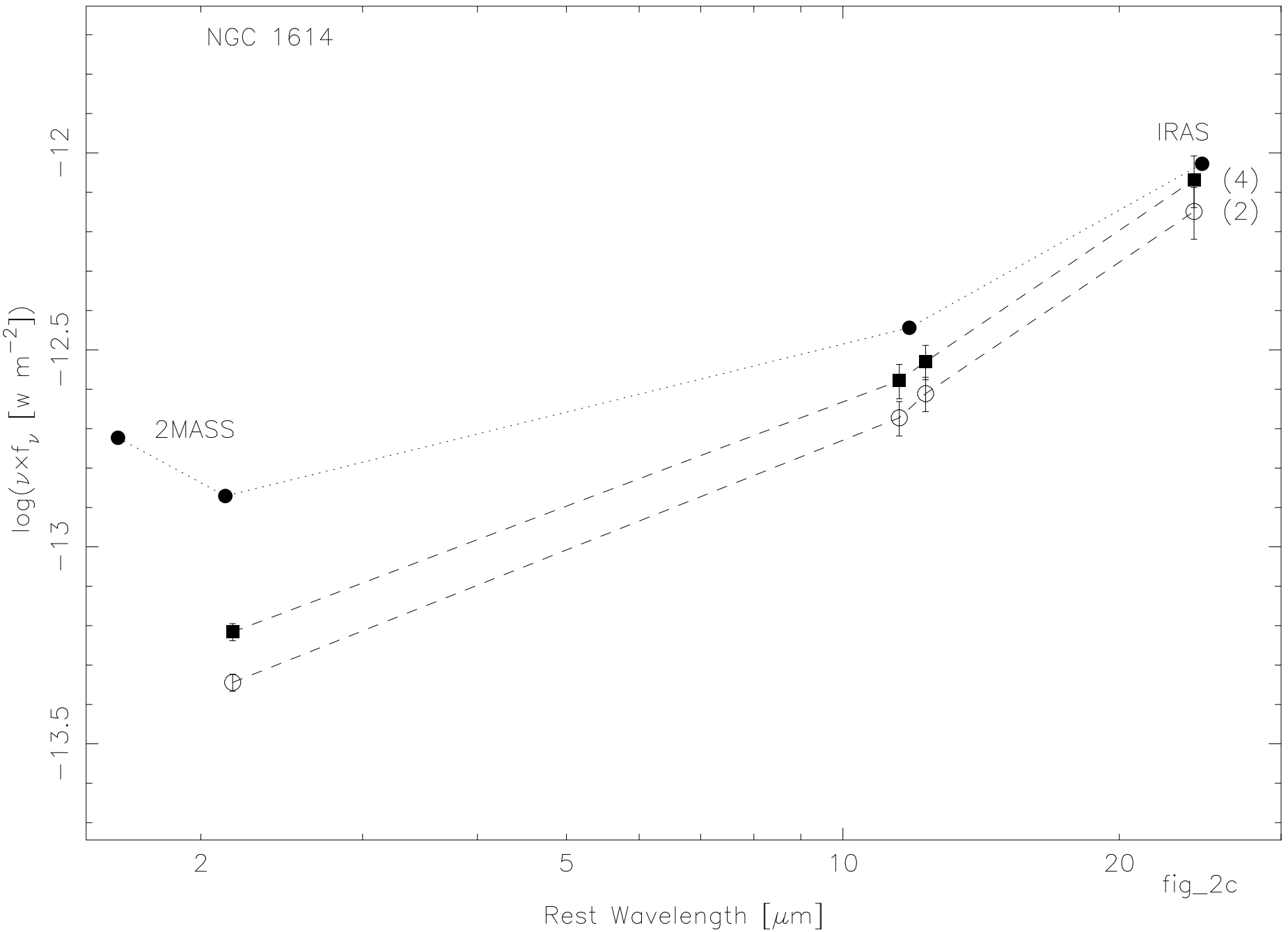
NGC 1614
IRAS
(4)
(2)
2MASS
−12
−12.5
−13
−13.5
log(ν×f_ν [w m^−2])
2
5
10
20
Rest Wavelength [μm]
fig_2c

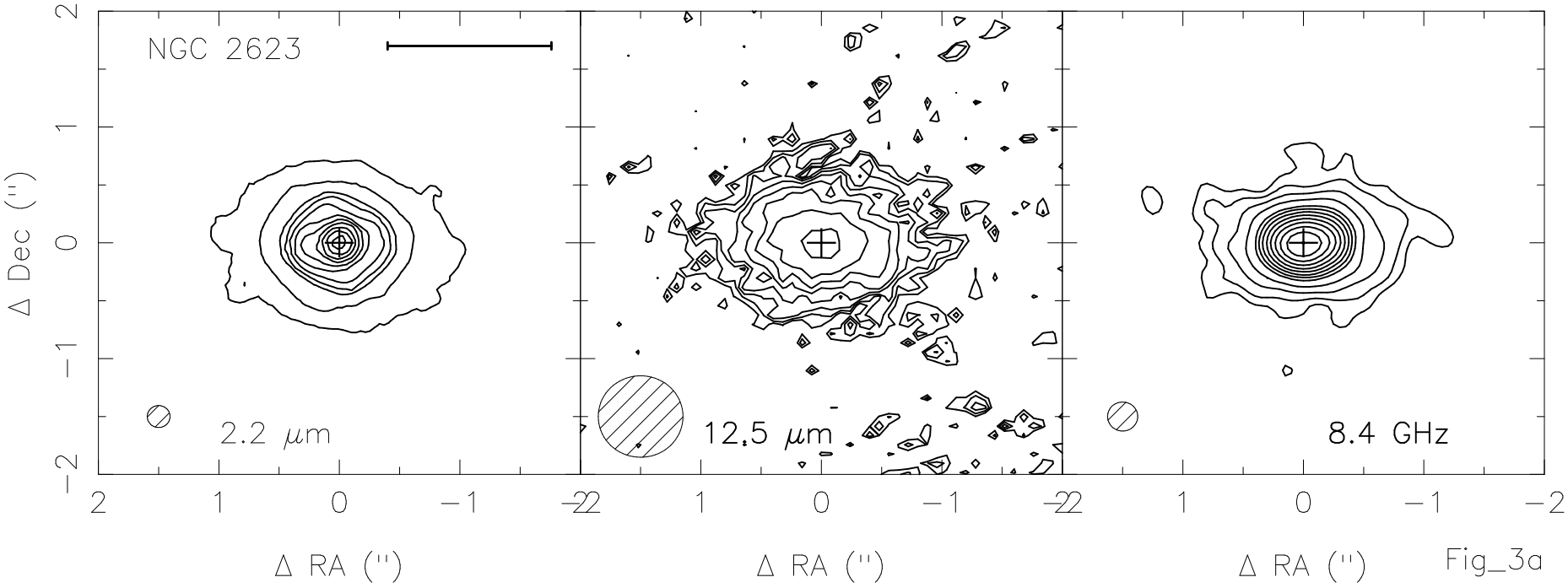

Fig_3a

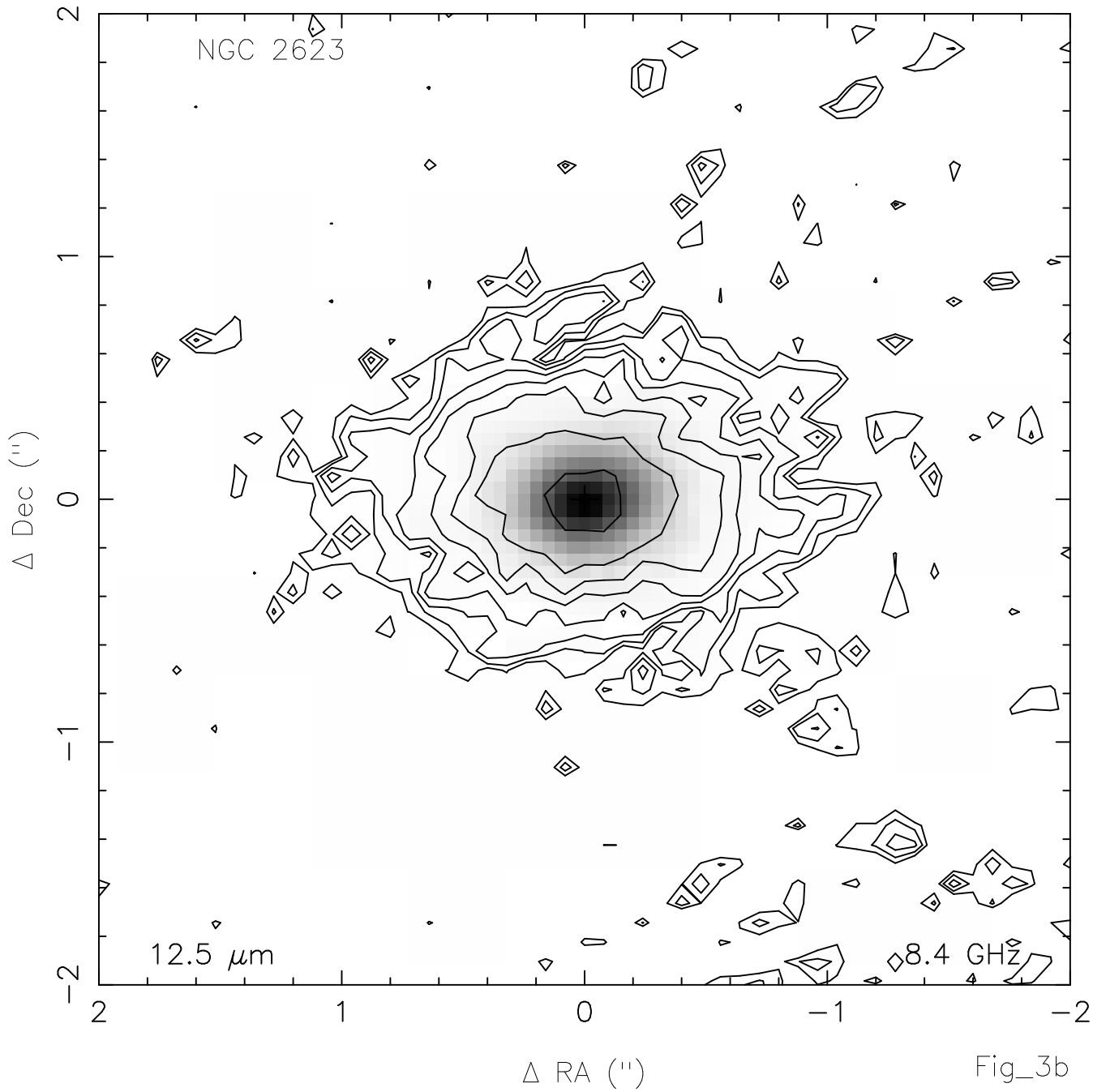

Fig_3b

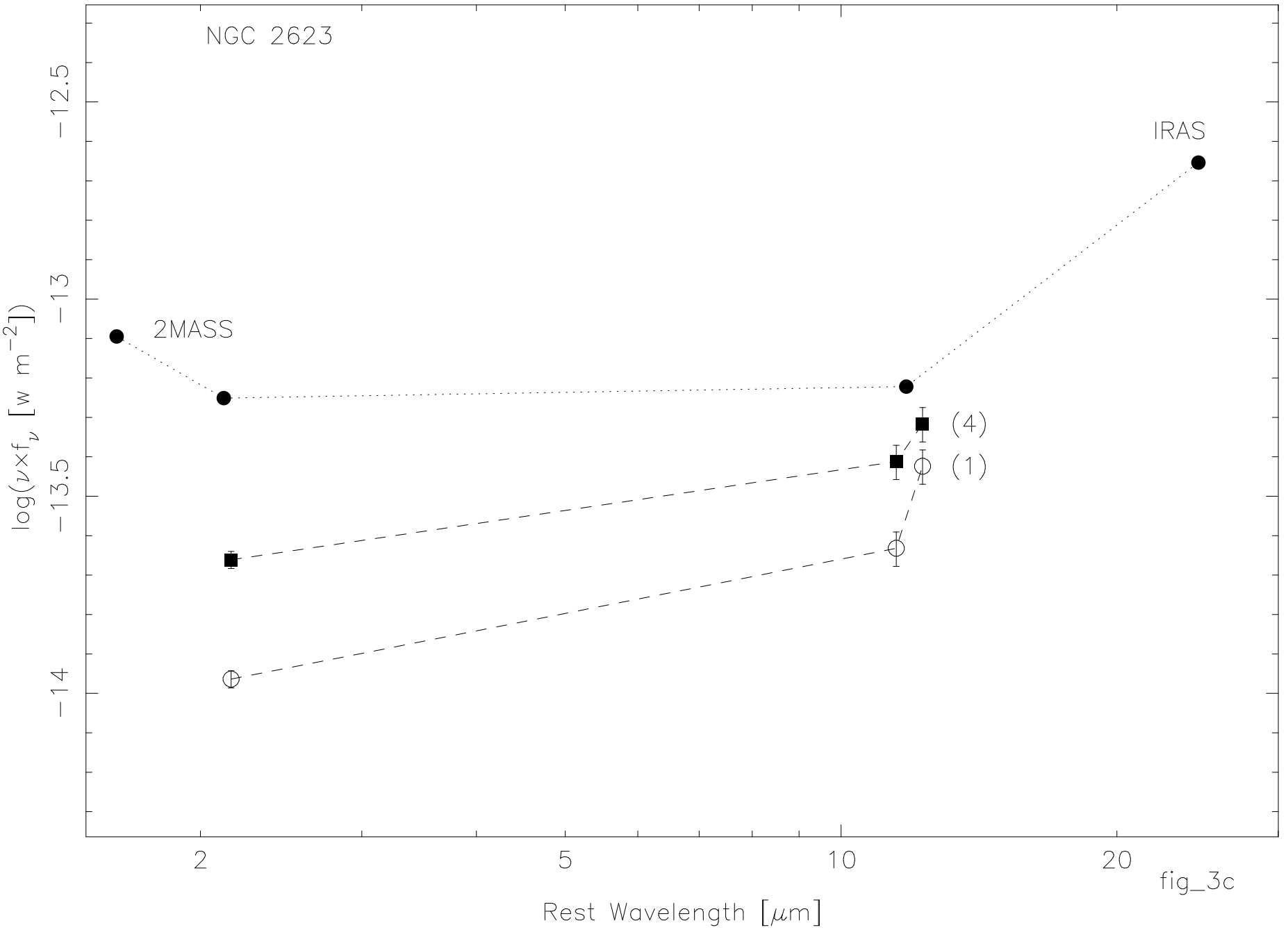
NGC 2623
IRAS
2MASS
(4)
(1)
−12.5
−13
−13.5
−14
log(ν×f_ν [w m^−2])
2
5
10
20
Rest Wavelength [μm]
fig_3c

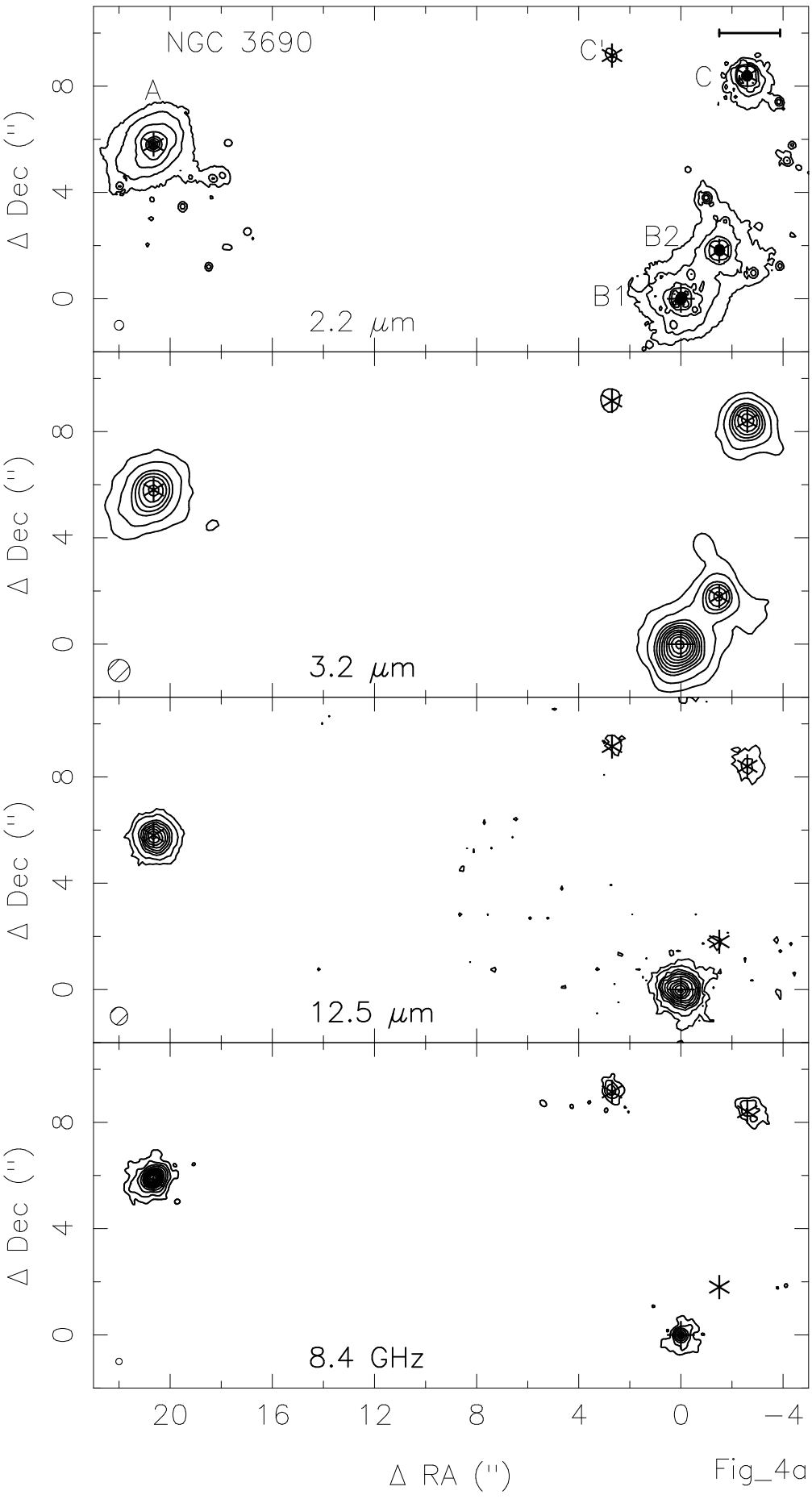
NGC 3690
A
C'
C
B2
B1
2.2 μm
3.2 μm
12.5 μm
8.4 GHz
Δ Dec (")
Δ RA (")
20
16
12
8
4
0
−4
0
4
8

Fig_4a

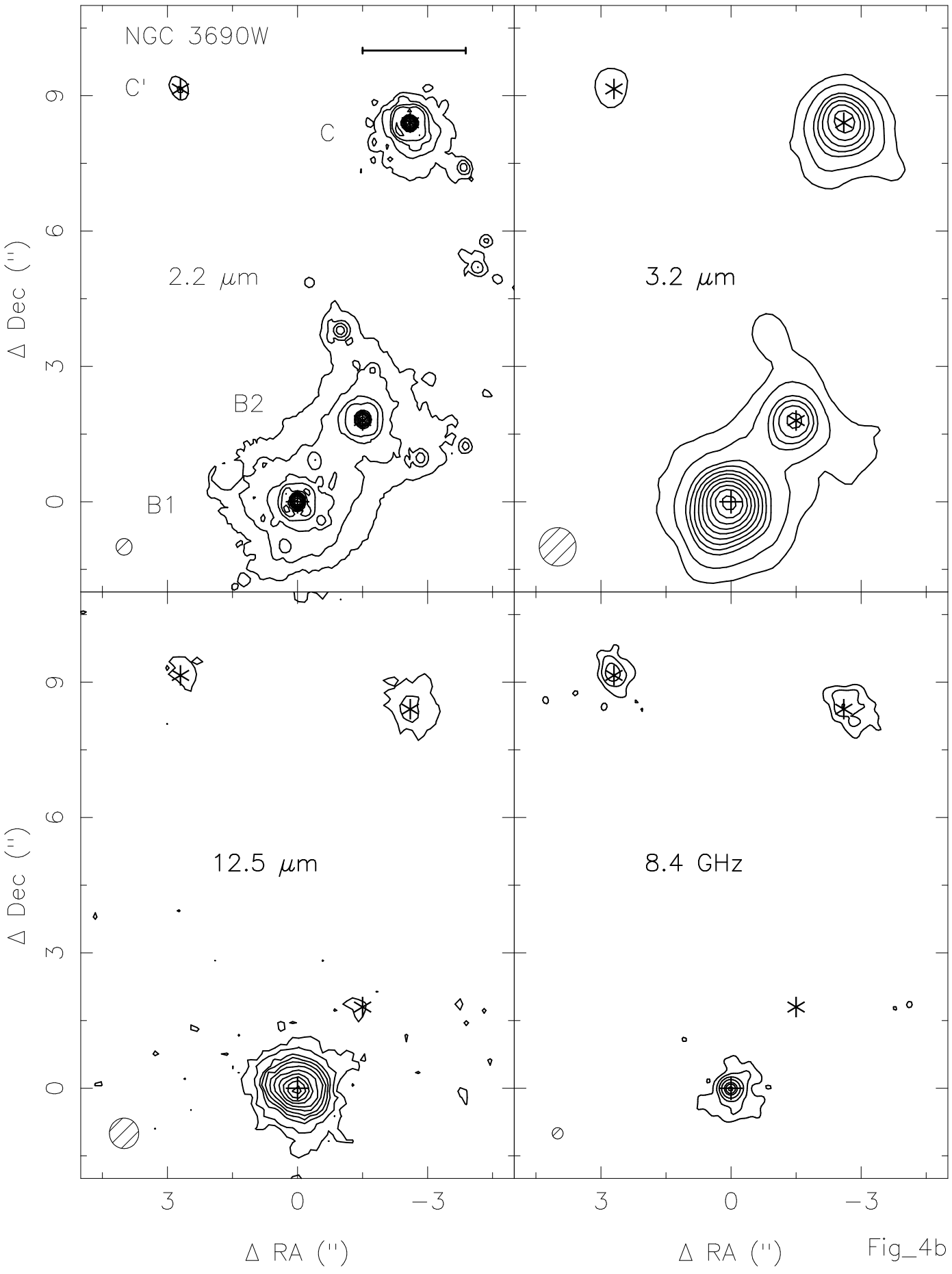

Fig_4b

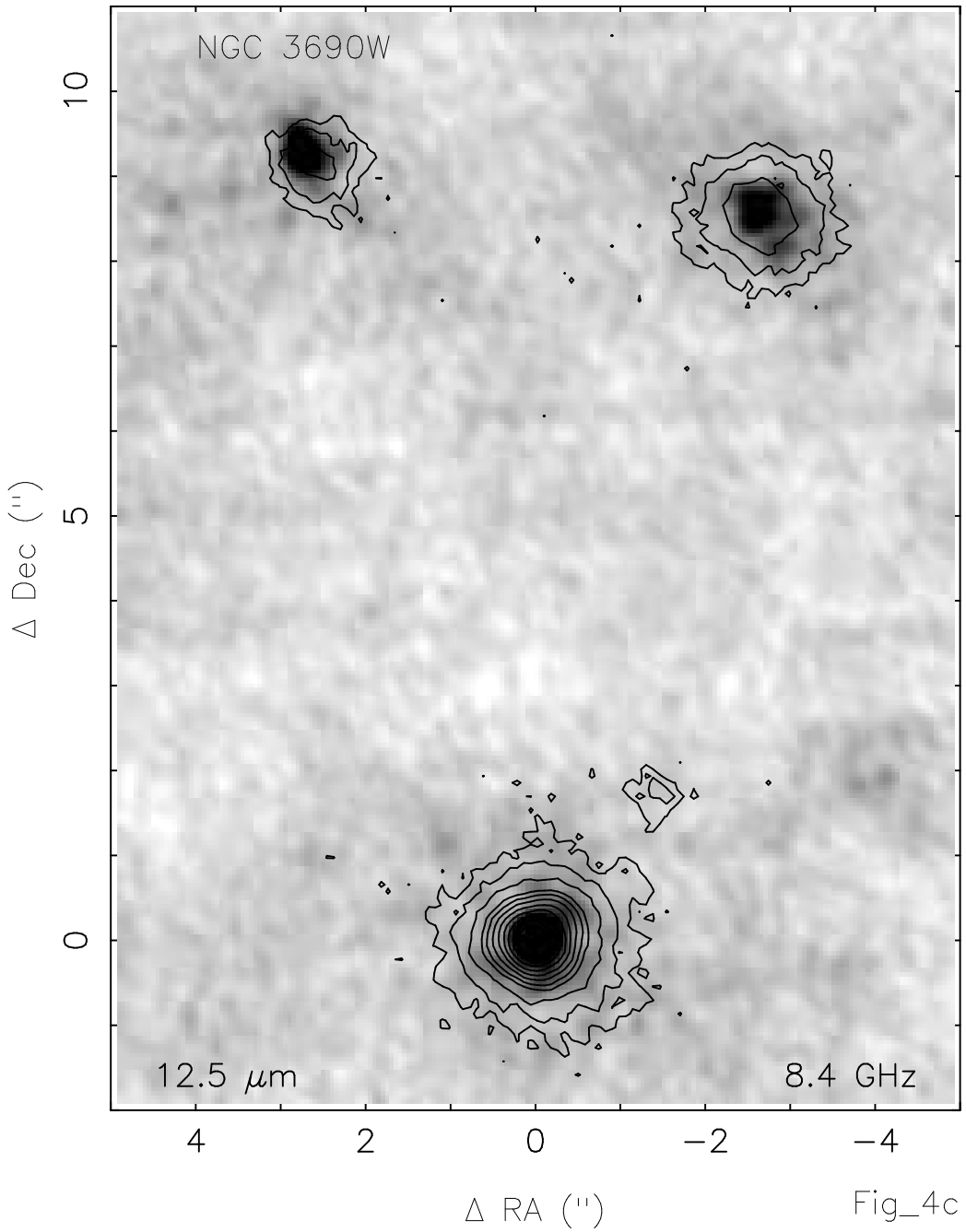

Fig_4c

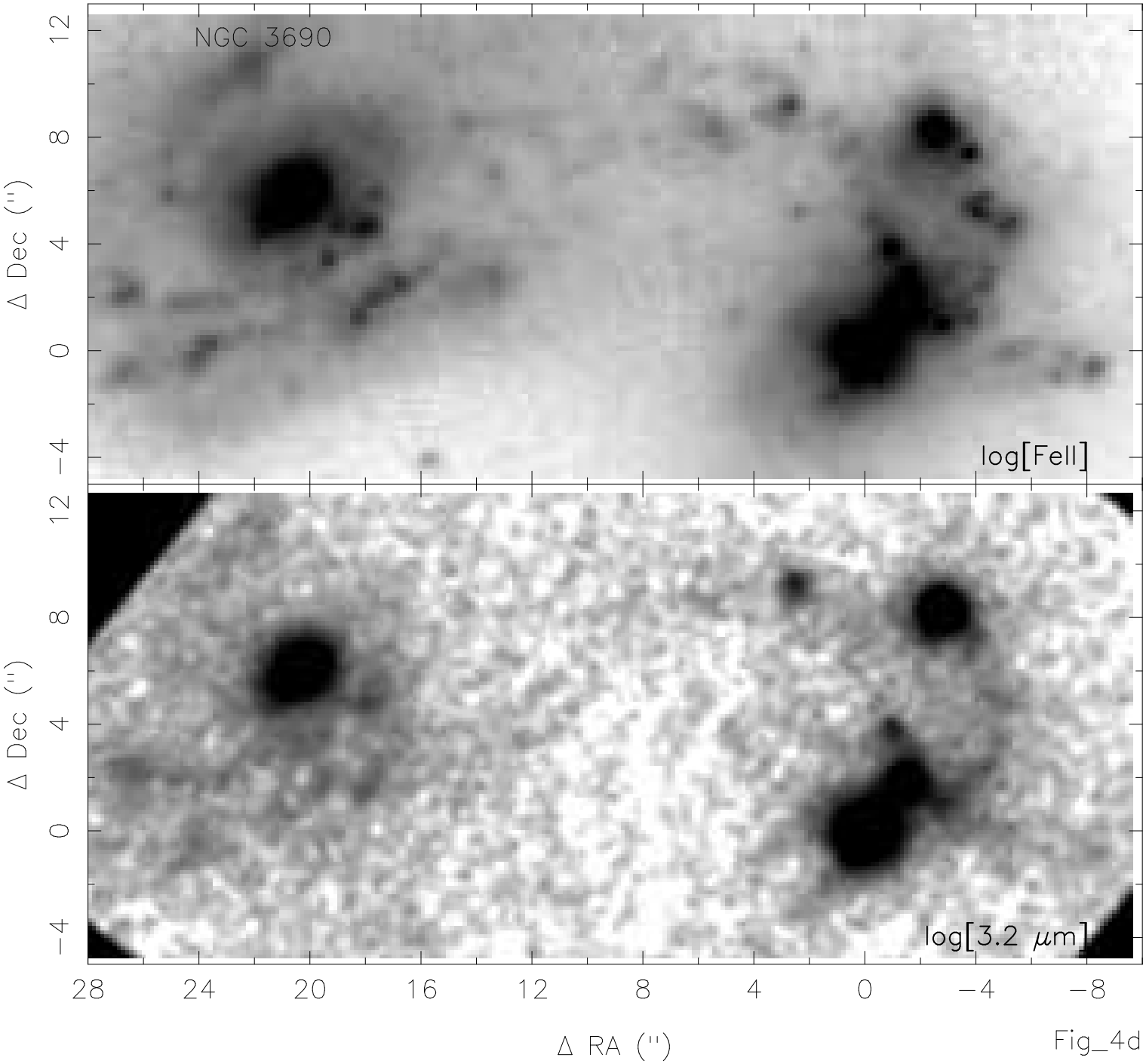

Fig_4d

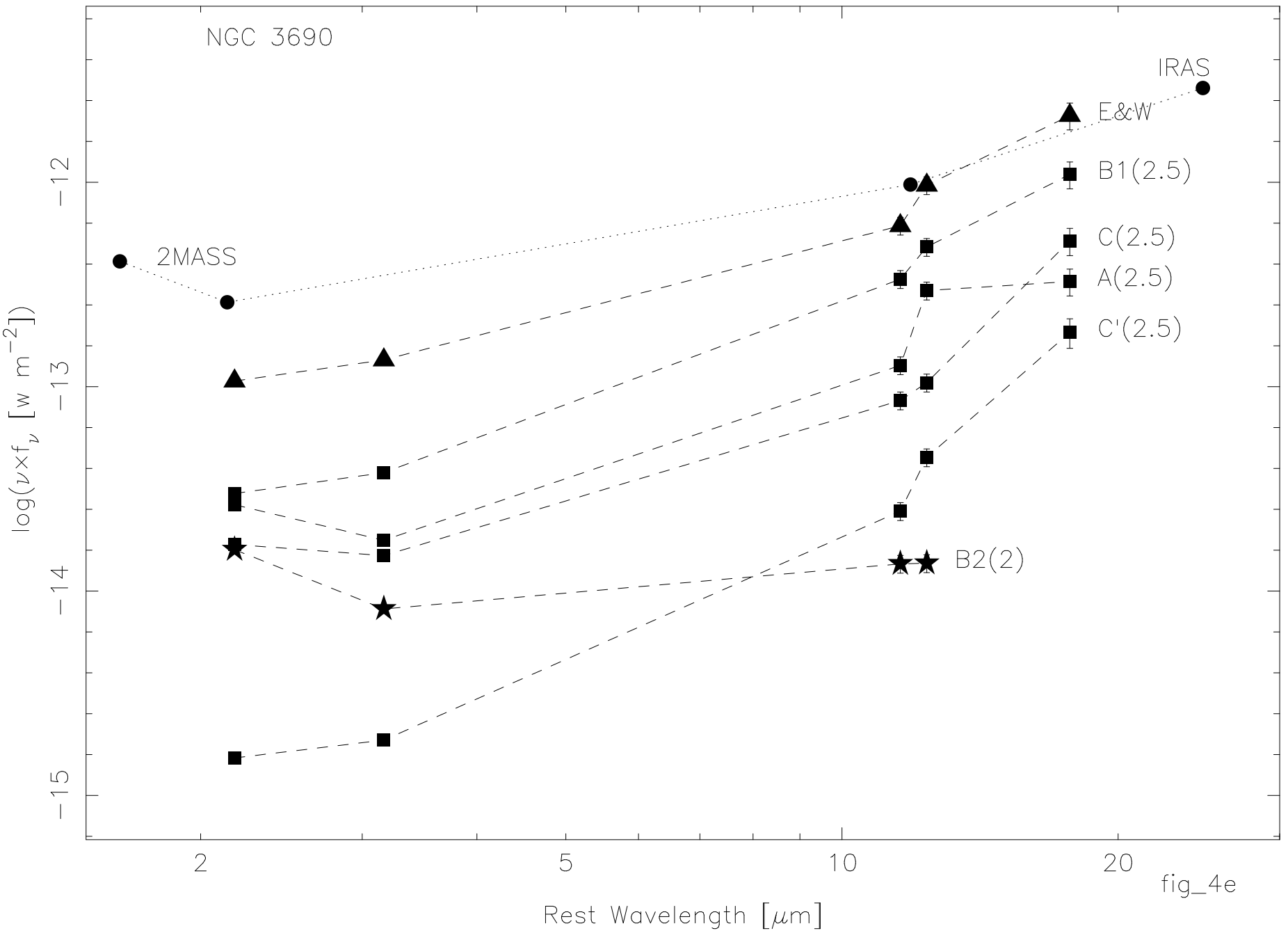
NGC 3690
IRAS
E&W
B1(2.5)
C(2.5)
A(2.5)
C'(2.5)
2MASS
B2(2)
−12
−13
−14
−15
log(ν×f_ν [w m^−2])
2
5
10
20
Rest Wavelength [μm]
fig_4e

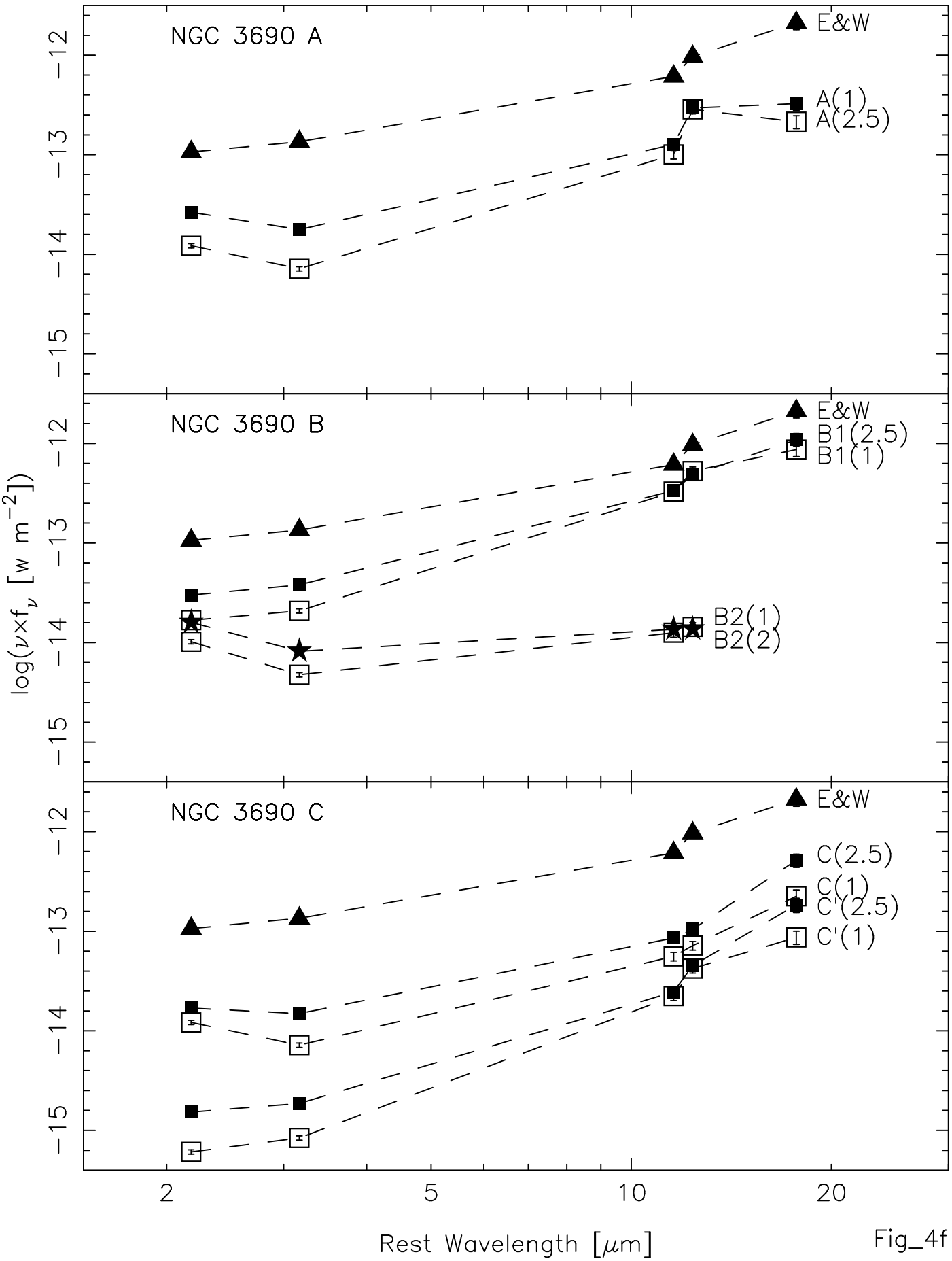
NGC 3690 A
E&W
A(1)
A(2.5)
NGC 3690 B
E&W
B1(2.5)
B1(1)
B2(1)
B2(2)
NGC 3690 C
E&W
C(2.5)
C(1)
C'(2.5)
C'(1)
log(νxf_ν [w m^-2])
−12
−13
−14
−15
2
5
10
20
Rest Wavelength [μm]

Fig_4f

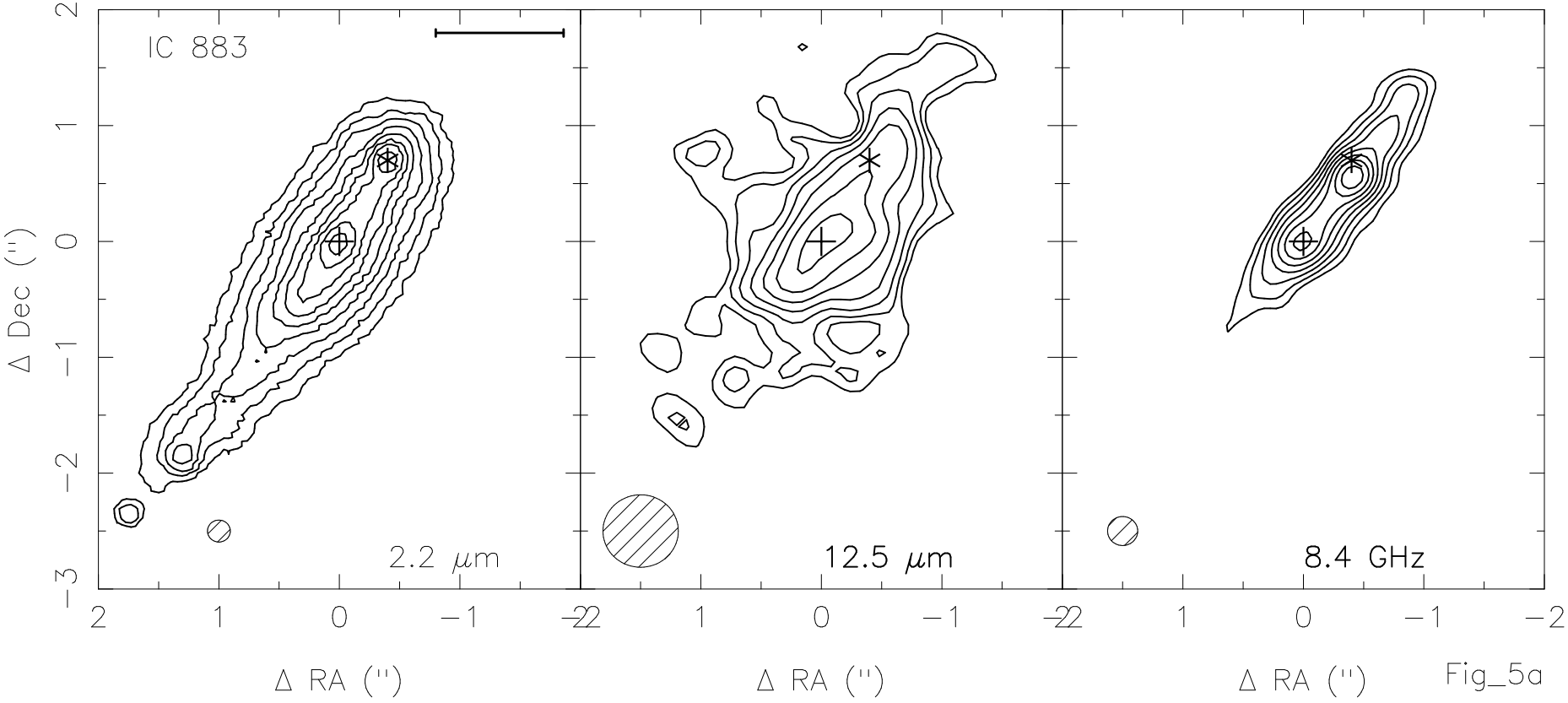

Fig_5a

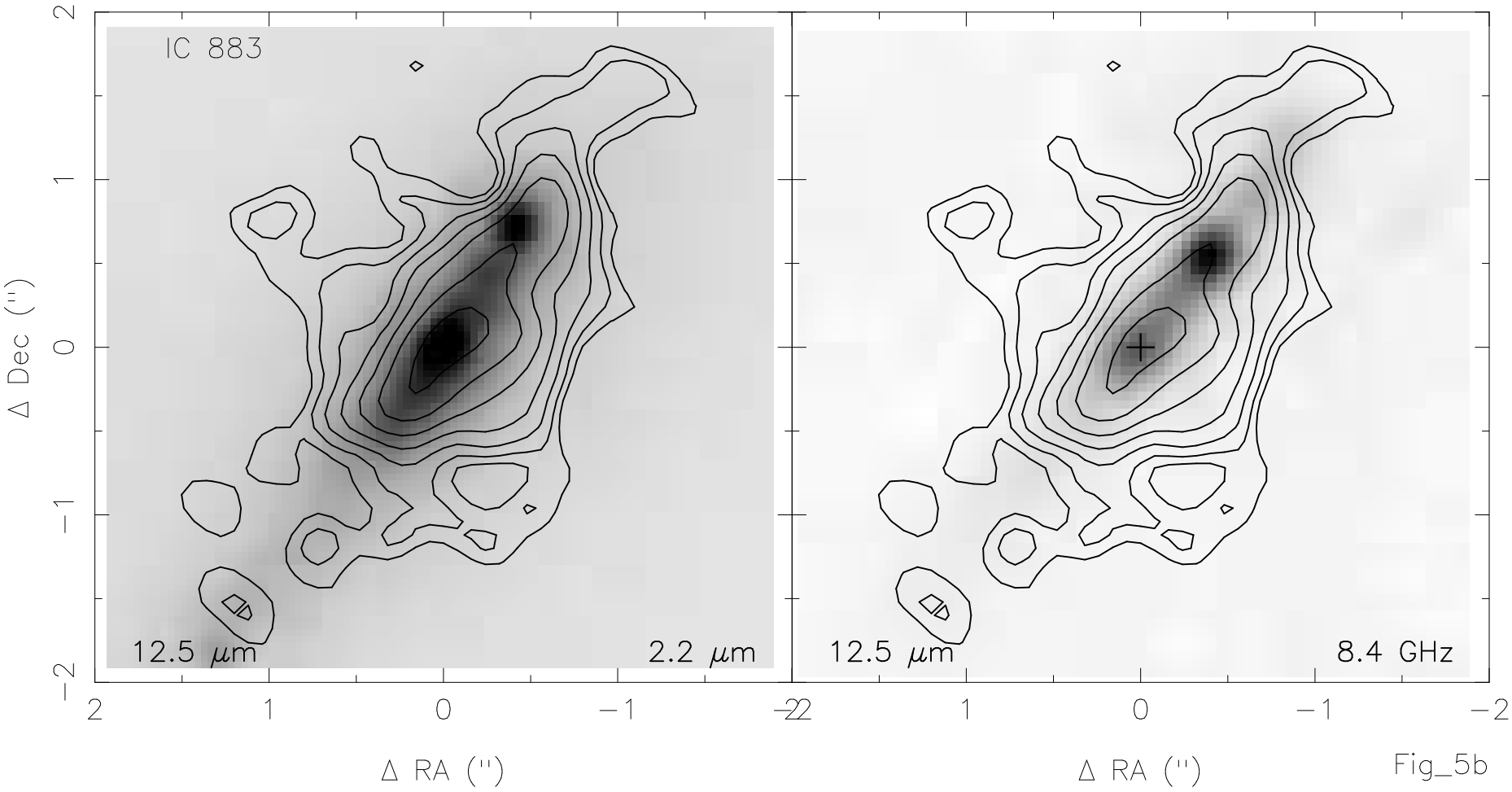

Fig_5b

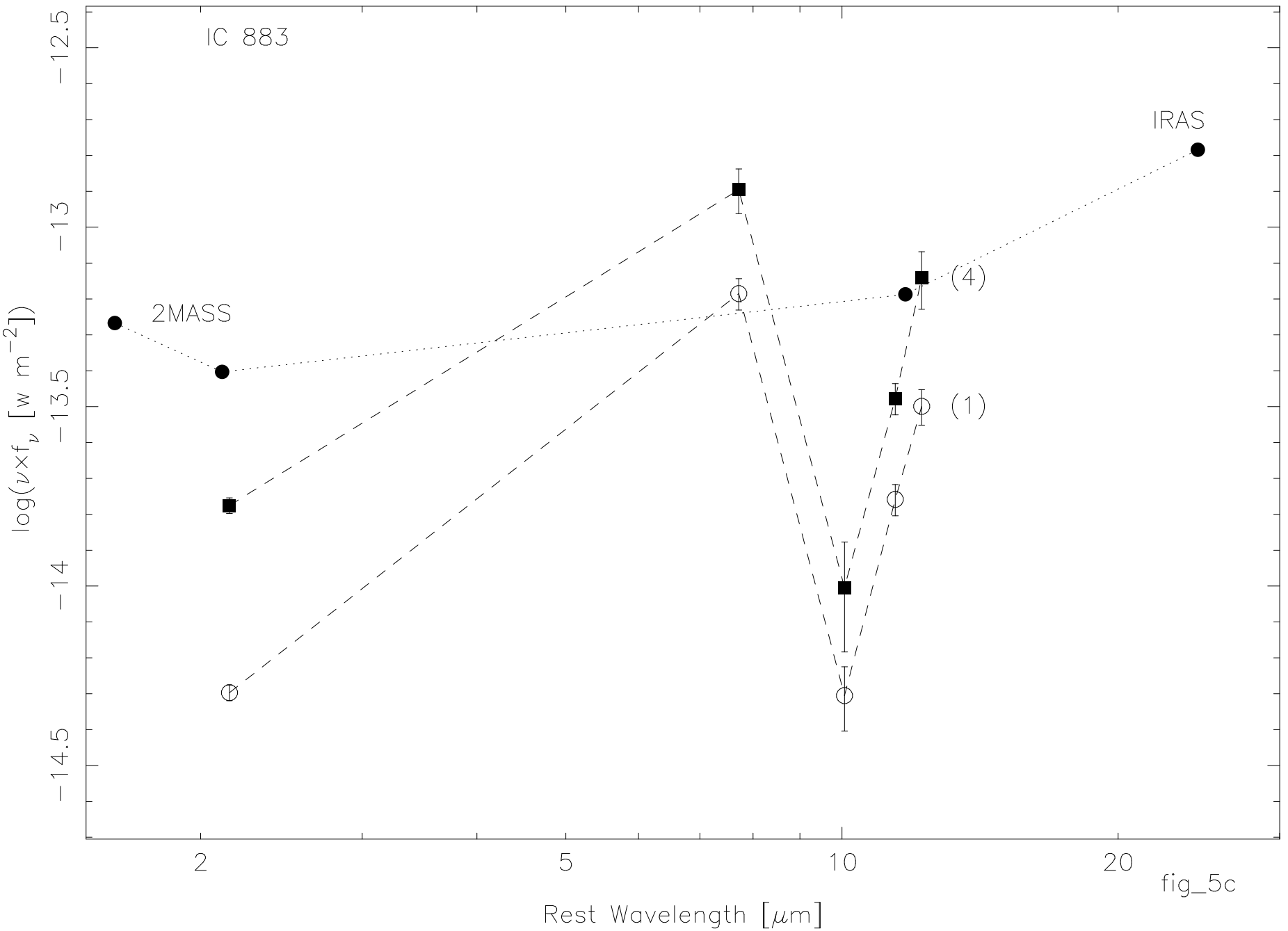
IC 883
IRAS
2MASS
(4)
(1)
−12.5
−13
−13.5
−14
−14.5
log(ν×f_ν [w m^−2])
2
5
10
20
Rest Wavelength [μm]
fig_5c

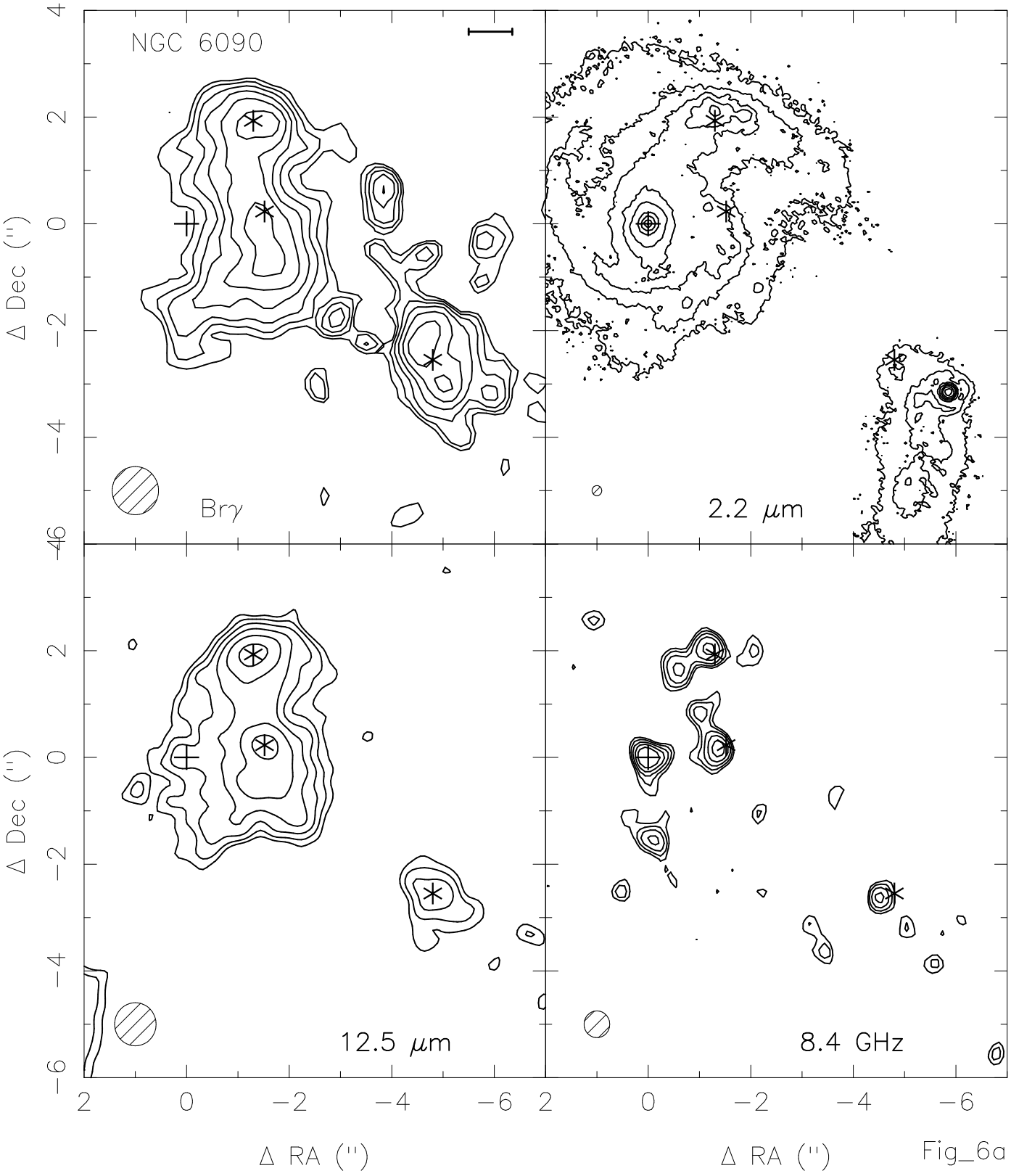

Fig_6a

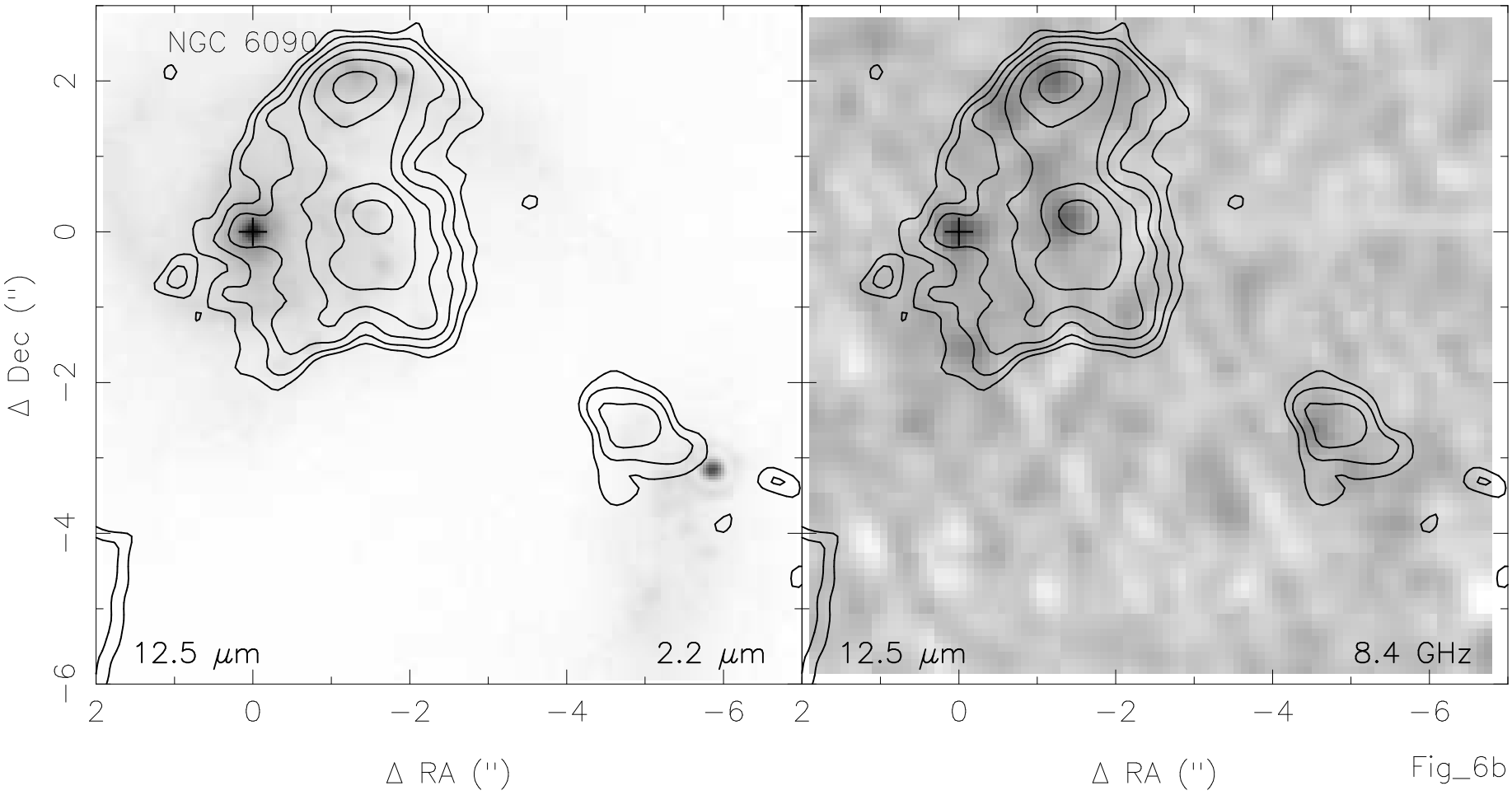

Fig_6b

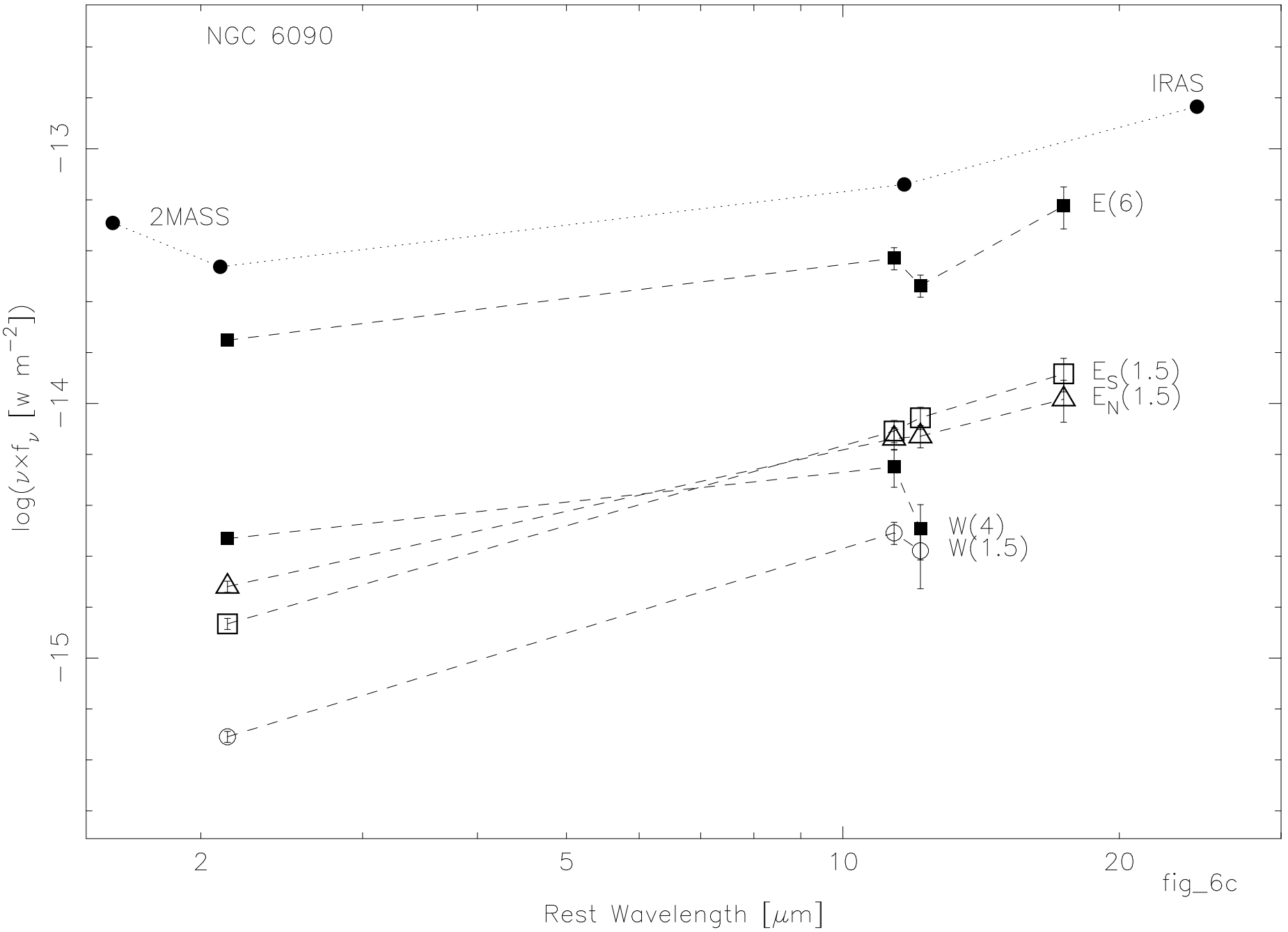
NGC 6090
IRAS
2MASS
E(6)
E_S(1.5)
E_N(1.5)
W(4)
W(1.5)
−13
−14
−15
log(ν×f_ν [w m^−2])
2
5
10
20
Rest Wavelength [μm]
fig_6c

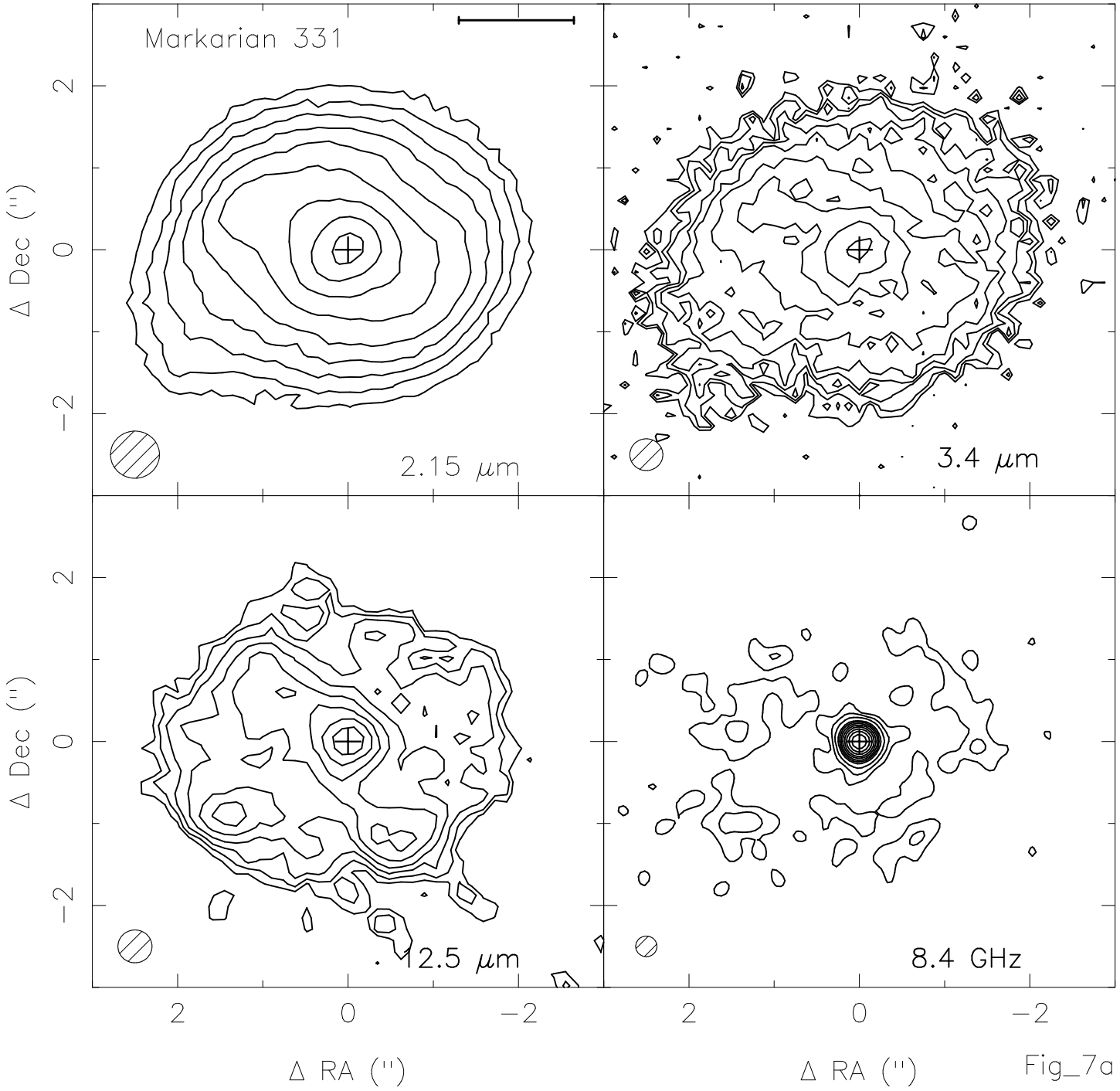

Fig_7a

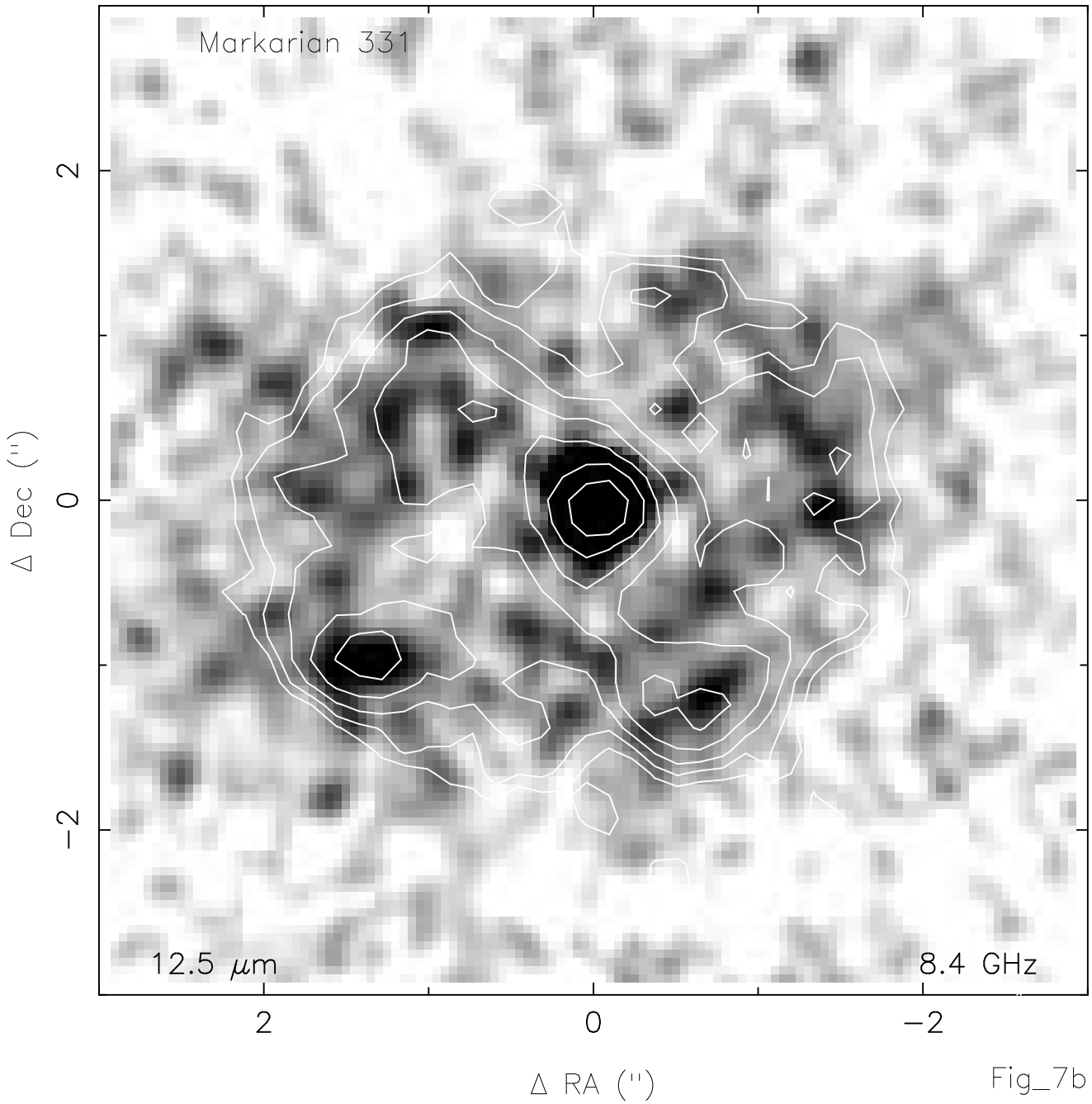

Fig_7b

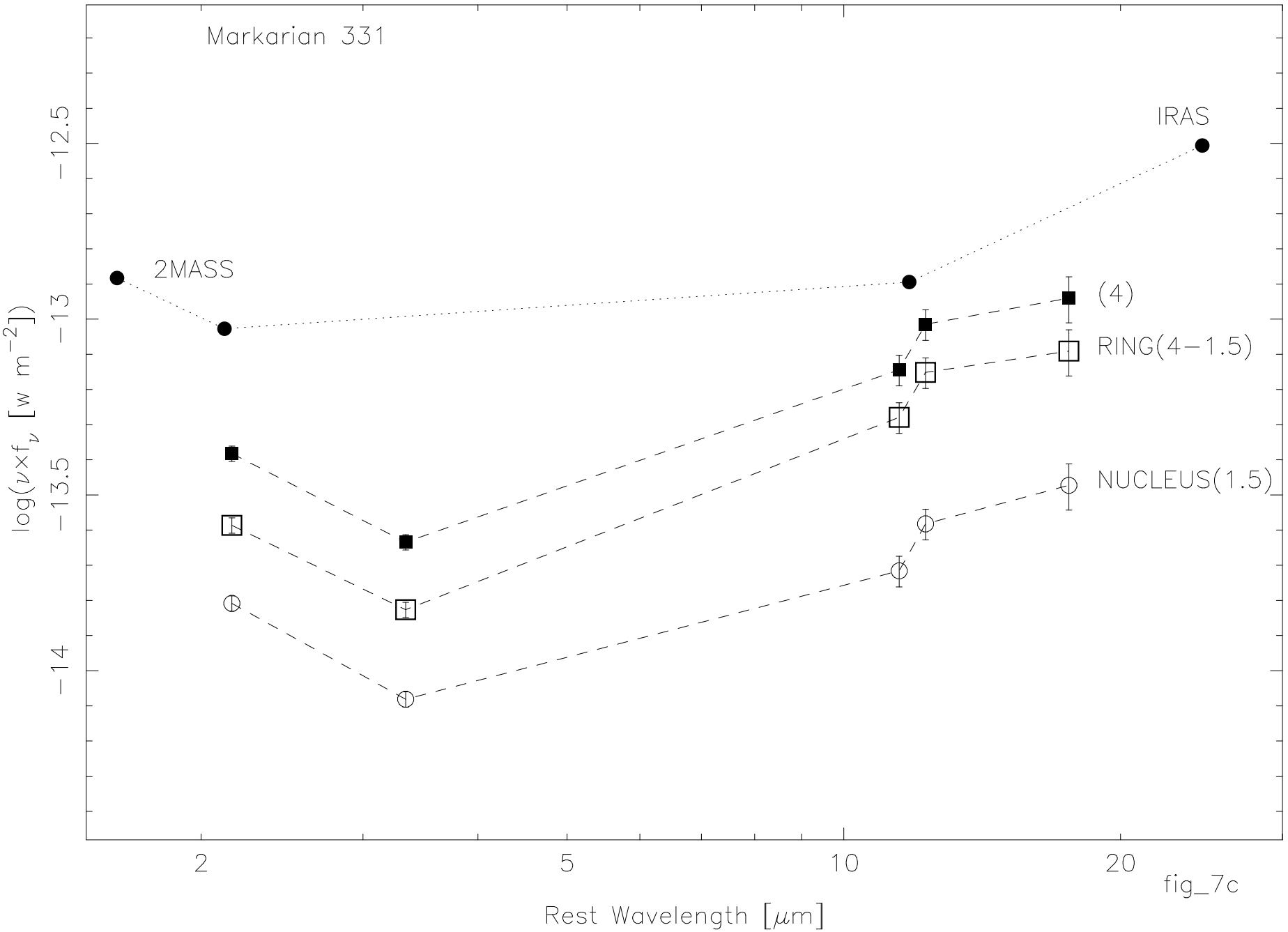
Markarian 331
IRAS
2MASS
(4)
RING(4−1.5)
NUCLEUS(1.5)
−12.5
−13
−13.5
−14
log(ν×f_ν [w m^−2])
2
5
10
20
Rest Wavelength [μm]
fig_7c

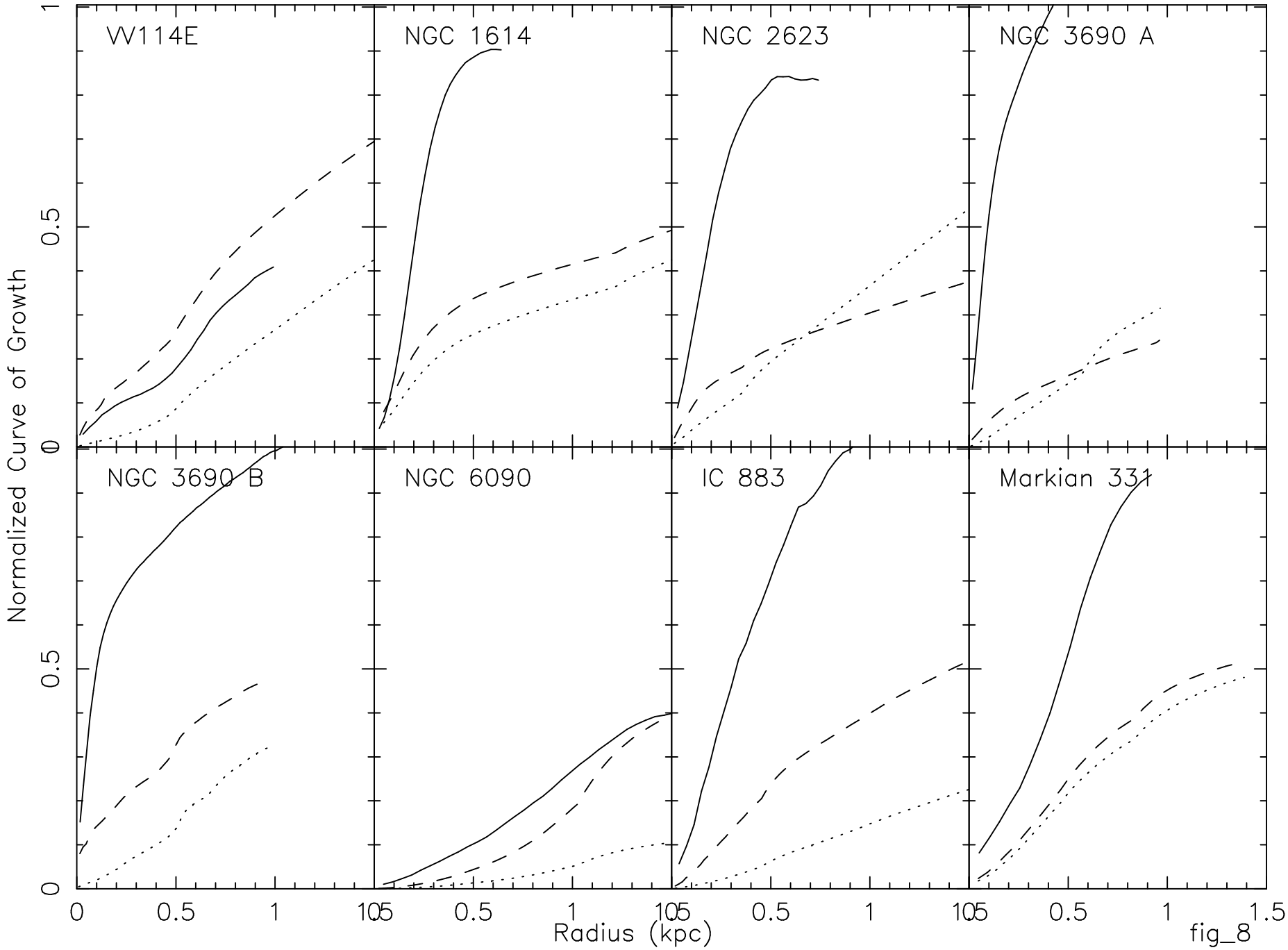
VV114E
NGC 1614
NGC 2623
NGC 3690 A
NGC 3690 B
NGC 6090
IC 883
Markian 331
Normalized Curve of Growth
Radius (kpc)
0
0.5
1
1.5
fig_8